

# Numerical Exploration of Planetary Arc Dynamics

BRUNO SICARDY

*Université Paris 7 et Observatoire de Paris, DAEC, 92195 Meudon Cédex Principal, France*

Received August 7, 1989; revised July 23, 1990

Ground-based observations have revealed in 1984 and 1985 the existence of interrupted ring-like structures, or “arcs” around Neptune. Recent observations by the Voyager 2 spacecraft in August 1989 have confirmed the presence of stable, dense arcs, embedded in a faint continuous ring. These structures would be destroyed in a few years if they followed unperturbed Keplerian motions. We study here the stabilizing effect of corotation and Lindblad resonances on planetary arcs, along the lines of previous analytical work by Lissauer (*Nature (London)* 318, 1985, 544–545) and Goldreich, Tremaine, and Borderies (*Astron. J.* 92, 1986, 490–494). We first describe analytically the response of a test particle to the combined effects of corotation and Lindblad resonances, caused by Neptunian satellites. The evolution of the particle is shown to be described by two coupled dynamical systems, the coupling depending on collective effects in the arc. This yields a formula for the energy provided by the Lindblad resonance, which is actually used to confine the arc material around the corotation resonance radius. We show in particular that the gradient of the torque density across the arc must be negative for the latter to be stable. This confirms in a general framework the constraints, previously given by Lin, Papaloizou, and Ruden (*Mon. Not. R. Astron. Soc.* 227, 1987, 75–95), on the relative positions of the corotation and the Lindblad resonances for the arc to be stable. We test our results with a direct numerical simulation, which takes into account inelastic collisions between identical spherical particles. Two configurations are studied: (1) an arc at a  $L_4$  Lagrange point of a satellite, further perturbed by an isolated Lindblad resonance with a second satellite, and (2) an arc at an isolated corotation resonance with a single satellite on an eccentric orbit. Our main results are: (a) the corotation points alone are unstable against dissipative collisions, (b) a stable arc must be submitted to a negative gradient of torque density, and (c) such a stable arc reaches a limit cycle where the energy provided by the resonant satellite is balanced by the energy dissipated by collisions. © 1991 Academic Press, Inc.

## 1. INTRODUCTION

Ground-based observations of stellar occultations by Neptune have shown in 1984 and 1985 that this planet is surrounded by incomplete ring-like structures, or “arcs” (Hubbard *et al.* 1986, Brahic *et al.* 1986, Sicardy *et al.*

1985, 1988). The radial width of the detected structures is 15 km, and the normal optical depth is in the range 0.06–0.075 (Nicholson *et al.* 1990, Sicardy *et al.* 1991).

The recent observations of the Voyager 2 spacecraft, during the encounter with Neptune in August 1989, has confirmed the existence of the arcs, and has also revealed a more complete ring system around the planet (Smith *et al.* 1989). More precisely, it appears that Neptune possesses two narrow rings at a distance of about 53,200 and 63,000 km from the planet center. Furthermore, a faint sheet of material (the “plateau”) extends from the inner ring to the middle of the two rings, and a diffuse, resolved ( $\Delta r \sim 1700$  km) ring lies around the 42,000-km radius. Embedded in the 63,000-km ring are three conspicuous, denser, arc structures, extending over a total azimuthal range of  $35^\circ$ , and spanning each  $4^\circ$ ,  $4^\circ$ , and  $10^\circ$ , from the leading to the trailing structure, respectively. Both the radial location and optical properties of these arcs are compatible with the ground-based observations. Finally, the extrapolation of the arc mean motion to the longitude of the 1984 and 1985 observations indicates that these structures are stable over a scale of at least 5 years (Smith *et al.* 1989).

The mere existence of the arcs requires an azimuthal confining mechanism, since the sidereal period of two particles at the inner and outer edges of the arc is of the order of 4 years. Some models have been proposed to account for the stability of arcs against the spreading effect of differential Keplerian motion. Basically, all these models involve a corotation resonance with a small satellite of Neptune. Corotation resonances with an eccentric satellite have been shown to azimuthally confine test particles (Dermott 1984). However, such a mechanism alone is unstable against the dissipative effect of inelastic collisions, since corotation points are local potential maxima. Lissauer (1985) proposed that particles could be trapped near the  $L_4$ , or  $L_5$ , stable Lagrange point of a satellite, while a second moon balances the dissipated energy through a series of overlapping Lindblad resonances. Goldreich, Tremaine, and Borderies (1986) have devel-

oped an alternative model where the corotation and the Lindblad resonances are generated by a *single* satellite with an eccentric or inclined orbit. The stability of ring-like arcs have been numerically tested by Lin, Papaloizou, and Ruden (1987), who insisted on the importance of the position of the Lindblad resonance with respect to the arc.

In this paper, we derive in a general framework the equations of motion of a particle trapped at a corotation resonance, and perturbed by a nearby Lindblad resonance. We show that the two-degrees of freedom motion of the particle may be described by two coupled, one-degree of freedom dynamical systems. The coupling between the two motions occurs because of collective effects in the arc and is eventually responsible for the stability, or instability, of the entire structure. In a second part of the paper, we test our results thanks to a direct simulation. Our code describes the 3-D motion of  $N$  identical spherical particles, inelastically colliding between themselves. Because collisions are difficult to handle properly in a mathematical framework, this kind of simulations may cast some light on the combined role of resonances and collisions in planetary rings. We explore in particular the arc dynamics by changing parameters like the masses and orbital elements of the satellites, the particle size, and the relative location of the resonances.

A preliminary analysis of the Voyager 2 observations does not show any obvious satellite candidate for creating corotation resonances at the arc location (Smith *et al.* 1989). We feel, however, that the present work may be useful in several aspects. First, a more careful data processing may unveil smaller satellites, dynamically linked with the arcs through corotation resonances. Second, and more important, the mechanism studied here is pretty general, and the equations describing it are sufficiently versatile to be accommodated to various problems of interest in the Solar System, all involving corotation resonances. One of them is the origin and the evolution of the Trojan asteroids, while further examples are given by the coorbital companions of Saturn's satellites Dione and Thetys. More generally, corotation points are natural sites where matter can be confined. Neptune's arcs, because they are inside the Roche limit of the planet, thus could be a "frozen" view of an important intermediate stage of the accretion process.

The general organization of this paper is as follows. Section 2 presents a heuristic discussion about the combined effects of corotation and Lindblad resonances on a test particle. Section 3 gives the equations of motion for a particle near corotation and Lindblad resonances and analyzes the coupling between the two phenomena in the presence of collective effects. Order of magnitude calculations are presented in Section 4. Section 5 briefly describes the simulation, and Section 6 presents the nu-

merical results. Concluding remarks are given in Section 7. Appendix A gives a list of the symbols used in the text.

## 2. COROTATION AND LINDBLAD RESONANCES

In the models so far proposed, the stability of an arc depends on the balance between three basic ingredients: (i) a corotation resonance, (ii) a Lindblad resonance, and (iii) collective effects with dissipation of energy.

We first discuss the combined effect of corotation and Lindblad resonances on a single particle. Consider a test particle  $T$  orbiting a central planet, of mass  $M_p$ , and perturbed by a satellite  $S$ , of mass  $M_s$ . Let  $R$  be the frame whose origin  $O$  is fixed at the planet center, while the axes remain parallel to themselves as the planet revolves around the planet-satellite center of mass. The potential  $\Phi$ , per unit mass, acting upon the particle in  $R$  is  $\Phi(\vec{r}, \vec{r}_s) = -GM_p/r + \Phi_s(\vec{r}, \vec{r}_s)$ , where the disturbing potential  $\Phi_s$  reads:

$$\Phi_s = \frac{GM_s}{r_s} \cdot \left( \frac{\vec{r} \cdot \vec{r}_s}{r_s^2} - \frac{r_s}{\Delta} \right), \quad (1)$$

where  $G$  is the gravitational constant,  $\vec{r}$  (resp.  $\vec{r}_s$ ) is the particle (resp. the satellite) position vector in  $R$ , and  $\Delta = |\vec{r} - \vec{r}_s|$ . Consider now the motion of  $T$  in the frame  $R'$  whose origin is  $O$ , but which rotates at the particle's mean motion,  $\langle n \rangle$ . The potential  $\Phi'$  acting upon  $T$  in  $R'$  is then

$$\Phi'(\vec{r}, \vec{r}_s) = -\frac{GM_p}{r} - \frac{\langle n \rangle^2 r^2}{2} + \Phi_s, \quad (2)$$

where  $-\langle n \rangle^2 r^2/2$  is the centrifugal potential. The unperturbed potential in  $R'$ , i.e.,  $-GM_p/r - \langle n \rangle^2 r^2/2$  exhibits a maximum, or "crest," at  $r = (GM_p/\langle n \rangle^2)^{1/3}$ . This radius corresponds to equilibrium points in  $R'$ , and separates prograde and retrograde circular orbits (Fig. 1a).

### 2.1. Corotation Resonances

If the satellite orbit is closed, as seen in  $R'$ , the averaged disturbing potential  $\langle \Phi_s \rangle$  is stationary in  $R'$ , and a *corotation* resonance occurs (here and thereafter, "averaged" means "averaged over a sidereal period between the particle and the satellite"). In this case, the mean effect of the satellite is to azimuthally modulate the crest of potential considered before, leading to local *maxima* of potential energy (or "hills"), separated by saddle points. Note that *no* local potential minima can be created in this way in the corotating frame  $R'$ . Three cases of corotation resonances may be envisaged (Fig. 1).

*Case (I).* The particle shares the satellite orbit. A few level curves of  $\langle \Phi_s \rangle$  are shown (Fig. 1b). One recognizes

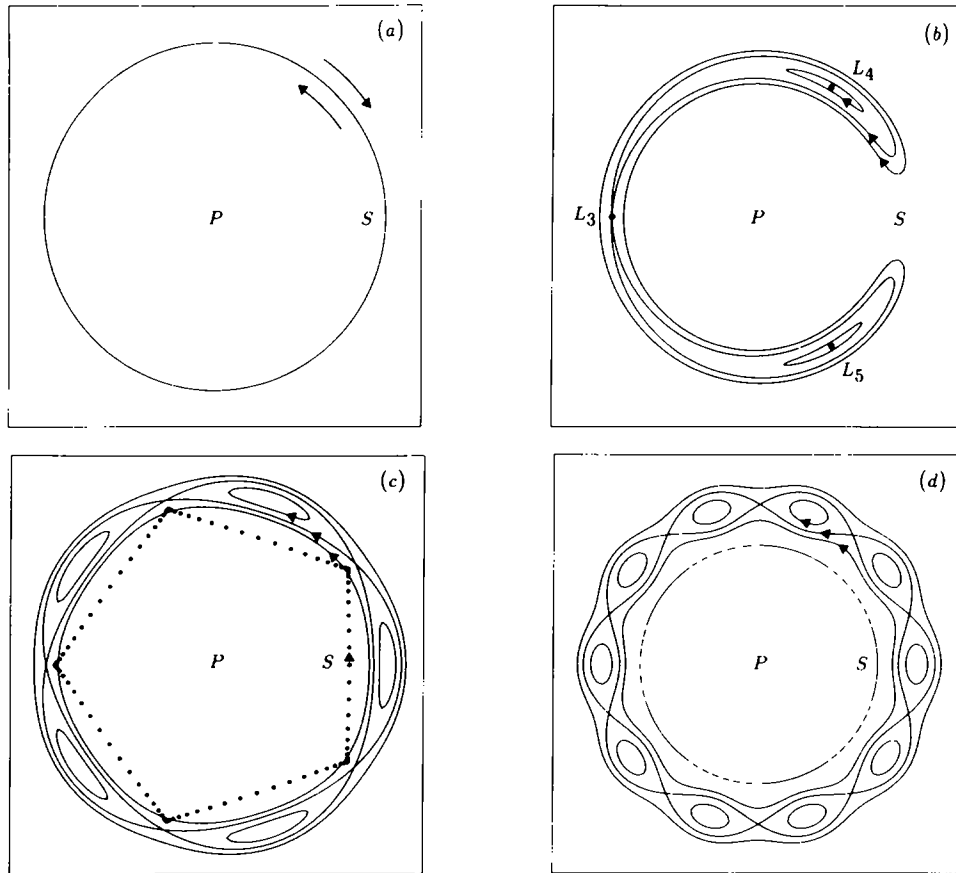


FIG. 1. Different illustrations of corotation resonances. The diagrams are drawn in a frame corotating with the mean motion of the test particle around the planet  $P$ . (a) In the absence of disturbing potential, the corotation circle (solid line) separates prograde and retrograde orbits (arrows). (b) The particle shares the orbit of the satellite  $S$ . The solid lines are examples of possible orbits followed by a particle (guiding center, tadpole, separatrix, and horseshoe).  $L_4$  and  $L_5$  are maxima of potential energy and  $L_3$  is a saddle point. The other two Lagrange points  $L_1$  and  $L_2$  are not shown here. (c) The same kind of topology is generated by a satellite with an eccentric orbit. The satellite position, as observed from the particle, is plotted at equal time intervals (dots). In this example,  $n/n_s = (m + 1)/m$  with  $m = -5$ , where  $n$  ( $n_s$ ) is the particle (the satellite) mean motion. (d) The corotation pattern generated by an inclined satellite. The inner circle is the satellite's orbit as viewed from the particle (solid line when the satellite is above the reference plane, dashed line when it is below). Again  $n/n_s = (m + 1)/m$  with  $m = -5$ .

the two stable Lagrange points  $L_4$  and  $L_5$ , corresponding to local maxima of potential energy, and the unstable Lagrange point  $L_3$ , corresponding to a saddle point.

*Case (2).* The ratio of the mean motion of the particle to that of the satellite is close to  $(m + 1)/m$ , where  $m$  is an integer:  $\langle n \rangle/n_s \sim (m + 1)/m$ , and the satellite orbit is eccentric. Then the satellite orbit is closed as seen in  $R'$ , and exhibits  $m$  lobes (Fig. 1c, see also Dermott 1984). The corotation potential is then composed of  $m$  hills in front of those points where the satellite orbit is farthest away from the particle orbit, and  $m$  saddle points in front of those points where the satellite is closest.

*Case (3).* Again  $\langle n \rangle/n_s \sim (m + 1)/m$ , but now the satellite's orbit is circular and inclined. Then the orbit exhibits  $2m$  arches, so that the potential felt by the particle in the corotating frame has  $2m$  maxima where the orbit of the satellite is farthest away (greatest elevation) and  $2m$  sad-

dle points where the satellite's orbit is closest (nodes, see Fig. 1d).

In all the three cases, the qualitative structure of the potential is the same: a series of hills of potential connected by saddle points. There is however an important difference between case (1) on one hand, and cases (2) and (3) on the other hand. In the first case, the disturbing potential due to the satellite is rigorously constant, but in the other two cases, only the *averaged* perturbing potential is constant while the satellite is moving along its orbit. In all cases, because of the Coriolis acceleration felt by the particle in the corotating frame, the particle undergoes an epicyclic motion whose guiding center follows the potential level curves instead of cutting them. Thus, the saddle points are unstable, and the potential maxima are shown to be stable, unless a dissipative force is present (see, e.g., Greenberg and Davis 1978).

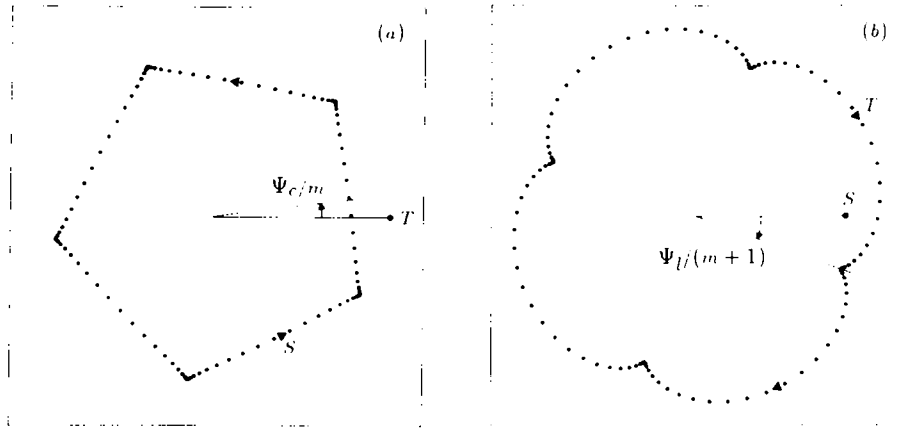


FIG. 2. (a) The geometrical interpretation of the corotation critical argument  $\Psi_c$ . The satellite position is plotted at equal time intervals, as seen from the test particle  $T$ . (b) The geometrical interpretation of the Lindblad resonance critical argument  $\Psi_l$ . The particle position is plotted at equal time intervals, as seen from the satellite. In both diagrams  $m = 5$  (see Fig. 1c).

Kinematic considerations show that the satellite's orbit is closed in  $R'$  if the corotation critical argument  $\Psi_c$  is stationary. The different expressions of  $\Psi_c$  are given in Table I, for the three cases presented here. In this table, and thereafter in this paper,  $\lambda(\lambda_s)$  is the particle (the satellite) mean longitude, and  $\tilde{\omega}_s$  and  $\Omega_s$  are the longitudes of the periapse and the node of the satellite's orbit. The geometrical interpretation of  $\Psi_c$  is given in Fig. 2a.

## 2.2. Lindblad Resonances

From a kinematic point of view, a Lindblad resonance is the symmetric configuration of a corotation resonance. Consider the motion of the particle  $T$  in a frame  $R''$  rotating with the satellite mean motion  $n_s$ . If the particle's orbit is closed in  $R''$ , then a *Lindblad* resonance occurs. Again, one can define a resonance critical argument  $\Psi_l$ , the expressions of which are given in Table I, where  $\Psi_{lh}$  is relevant for an eccentric particle's orbit (horizontal displacements), while  $\Psi_{lv}$  applies for an inclined orbit (vertical displacements). Finally,  $\tilde{\omega}$  and  $\Omega$  are the longitudes of the periapse and the node of the particle's orbit. The geometrical interpretation of  $\Psi_l$  is displayed in Fig. 2b.

## 2.3. Corotation vs Lindblad Resonances

The important property of corotation resonances is that they can force  $\Psi_c$ , and thus  $\lambda$ , to librate in a finite interval. In that sense, corotation radii are good candidates for arc location. On the other hand, the basic property of Lindblad resonances is that they allow a secular exchange of energy and angular momentum between the satellite and the particle (Goldreich and Tremaine 1980). This exchange occurs as soon as the critical argument  $\Psi_l$  is different from 0 or  $\pi$ , since the symmetry of the particle's orbit relative to the planet-satellite line is then destroyed (Fig.

2b). As noted by Goldreich, Tremaine, and Borderies (1986), when there is only one satellite responsible for the two resonances (cases 2 and 3), then the corotation condition  $\Psi_c \sim 0$  is met quasi-simultaneously with the Lindblad resonance condition  $\Psi_l \sim 0$ . This is because the Keplerian motion is degenerate, i.e.,  $\tilde{\omega}_s, \Omega_s, \tilde{\omega}, \Omega \ll n, n_s$  around a moderately oblate planet.

The problem we have to study is thus the three-body problem near a first order resonance, with an additional perturbation due to the planet oblateness. This dynamical system has two critical arguments ( $\Psi_c$  and  $\Psi_{lh}$ ), in the planar problem, and three critical arguments ( $\Psi_c$ ,  $\Psi_{lh}$ , and  $\Psi_{lv}$ ) in the 3-D case. This problem is further complicated by collective effects and dissipative processes, like inelastic collisions. We want to analyze the coupling between the different degrees of freedom of the system, and we want also to clarify the role of the dissipative processes on the long-term evolution of this system. Before embarking on the equations, we make some heuristic remarks on the interaction between the corotation and the Lindblad resonances.

Let  $E_i$  and  $H_i$  be the energy and angular momentum of the test particle  $T$  in the inertial frame  $R$ , and let  $\mathcal{E}$  be the energy of  $T$  in the corotating frame  $R'$ . If  $T$  is in Lindblad resonance with a satellite  $S$ , then  $\Delta E_i = n_s \Delta H_i$ , from the conservation of Jacobi constant. Furthermore,  $\mathcal{E} = E_i - nH_i$ , thus

$$\Delta \mathcal{E} = (n_s - n) \Delta H_i. \quad (3)$$

In the presence of collective effects and/or dissipation of energy, the net effect of the Lindblad resonance is a secular exchange of energy and angular momentum between the satellite and the particle (Goldreich and Tremaine 1982). In all the cases, the satellite tends to push the

TABLE I  
Arguments and Functions of the Disturbing Potential

	Case 1	Case 2	Case 3
$\Psi_c$	$\lambda - \lambda_s$	$(m + 1)\lambda_s - m\lambda - \bar{\omega}_s$	$2[(m + 1)\lambda_s - m\lambda - \Omega_s]$
$\Psi_{lh}$	$(m + 1)\lambda'_s - m\lambda - \bar{\omega}$	$(m + 1)\lambda_s - m\lambda - \bar{\omega}$	$(m + 1)\lambda_s - m\lambda - \bar{\omega}$
$\Psi_{lv}$	—	—	$2[(m + 1)\lambda_s - m\lambda - \Omega]$
$\mathcal{D}_c$	$\varepsilon\{\cos(\Psi_c) - 1/2 \sin(\Psi_c/2)\}$	$\varepsilon\beta E e_s \cos(\Psi_c)$	$-\varepsilon\beta V i_s^2 \cos(\Psi_c)$
$\mathcal{D}_{lh}$	$\varepsilon' \beta' A' e \cos(\Psi_{lh})$	$\varepsilon\beta A e \cos(\Psi_{lh})$	$\varepsilon\beta A e \cos(\Psi_{lh})$
$\mathcal{D}_{lv}$	—	—	$-\varepsilon\beta V i^2 \cos(\Psi_{lv})$
			$+ 2\varepsilon\beta i i_s \cos[(\Psi_c + \Psi_{lv})/2]$
$\mathcal{A}$	$-\frac{1}{2} \left[ \varepsilon' \beta' b_{1/2}^{(0)} + \left(\frac{R_p}{a}\right)^2 J_2 \right]$	$-\frac{1}{2} \left[ \varepsilon\beta b_{1/2}^{(0)} + \left(\frac{R_p}{a}\right)^2 J_2 \right]$	$-\frac{1}{2} \left[ \varepsilon\beta b_{1/2}^{(0)} + \left(\frac{R_p}{a}\right)^2 J_2 \right]$

Note.  $A = \frac{1}{2} \left[ 2(m + 1)b_{1/2}^{(m+1)} + \beta \frac{db_{1/2}^{(m+1)}}{d\beta} \right]$ .

$E = \frac{1}{2} \left[ (2m + 1)b_{1/2}^{(m)} + \beta \frac{db_{1/2}^{(m)}}{d\beta} \right]$ .

$V = \frac{1}{8} \beta b_{3/2}^{(2m+1)}$ .

particle away from its own orbit ("shepherding effect"), thus  $\Delta H_i > 0$  if  $n_s - n > 0$  and  $\Delta H_i < 0$  if  $n_s - n < 0$ . Consequently,  $\Delta \mathcal{E} > 0$  in all cases. A naive interpretation of this result may lead to the conclusion that the Lindblad resonance always compensates for the energy lost by collisions. The difficulty is, however, that part of the energy  $\mathcal{E}$  in the corotating frame is stored in the eccentricity of the particle orbit (i.e., kinetic energy in  $R'$ ), and another part is stored in the guiding center of the particle (potential energy, which is maximum at a stable corotation points, see above). As we shall see, *most* of the energy provided by the Lindblad resonance is used to excite the arc eccentricity, *not* to confine it near the corotation point. The distribution of energy between these two modes actually depends more subtly on the interactions between the particles, and more precisely, on collective effects (Section 3.4).

### 3. EQUATIONS OF MOTION

#### 3.1. Disturbing Potential

The disturbing potential  $\Phi_s$  given in Eq. (1) may be expressed in terms of the particle and the satellite(s) orbital elements, instead of being given in Cartesian coordinates. From now on, the orbital elements of the particle will be denoted  $a, e, i, \lambda, \Omega$ , and  $\bar{\omega}$ . The angular quantities  $\lambda, \Omega$ , and  $\bar{\omega}$  have already been defined in the previous section as the mean longitude, the longitude of the ascending node, and the longitude of the periaipse, respectively, while  $a, e$ , and  $i$  are, respectively, the semi-major

axis, the eccentricity, and the inclination. Quantities with subscript  $s$  or  $s'$  refer to the satellite  $S$  or  $S'$ , respectively.

The expansion of  $\Phi_s$  in terms of these orbital elements is described, e.g., in Peale (1986). It is convenient to use for this the ratio  $\varepsilon = M_s/M_p$  ( $\varepsilon' = M_{s'}/M_p$ ) of the satellite mass to the planet mass. Also used are the ratio  $\beta = a/a_s$  ( $\beta' = a/a'_s$ ), and the so-called Laplace coefficients  $b_\gamma^{(m)}(\beta)$ , whose basic properties are described by Brouwer and Clemence (1961); see also Shu (1984). Besides the effect of the satellite(s), we include in the disturbing potential the effect of the dynamical oblateness  $J_2$  of the planet, whose equatorial radius is denoted  $R_p$ . This oblateness yields axisymmetric perturbing terms in  $\Phi_s$ .

The potential  $\Phi_s$  is expanded to the first order in  $e$  and  $e_s$ , and to the second order in  $i$  and  $i_s$ . Furthermore, near a  $m : m + 1$  commensurability, only the axisymmetric terms and the terms containing the slowly varying critical arguments  $\Psi_c$  and  $\Psi_l$  are retained. The other high-frequency terms are assumed to average to zero over one sidereal period, leading to the so-called average disturbing potential  $\langle \Phi_s \rangle$ . The averaging of the elliptic problem near a first-order resonance  $m : m + 1$  is detailed, e.g., in Ferraz-Mello (1987). It leaves only the terms  $\mathcal{D}$  depending on the critical arguments  $\Psi_c$  and  $\Psi_l$ , plus an axisymmetric term  $\mathcal{A}$ :

$$\langle \Phi_s \rangle / (na)^2 = \mathcal{D}_c(\Psi_c) + \mathcal{D}_{lh}(\Psi_{lh}) + \mathcal{D}_{lv}(\Psi_{lv}) + \mathcal{A}. \quad (4)$$

The different expressions for the functions  $\mathcal{D}$  and  $\mathcal{A}$  are given in Table I. For order of magnitude considerations,

it is useful to note that in Table I, the dimensionless coefficient  $A$  is of order  $m$ , while  $E = O(-m)$ . Numerical integrations show that both  $A/m$  and  $-E/m$  tend to  $\sim 0.802 \dots$  as  $m$  goes to infinity.

### 3.2 Equations of Perturbation

The equations of motion are derived from the Lagrange equations of perturbation, using the averaged disturbing potential of Eq. (4). The following variables are used to describe the particle motion:

- $\xi = (a - a_0)/a_0$ , where  $a_0$  is a reference radius, chosen to simplify as much as possible the equations, once the axisymmetric terms due to the oblateness of the planet and the satellite orbits are taken into account (Peale 1986). The quantity  $a_0$  may be viewed as the corotation radius, so that  $\xi$  is the dimensionless distance to corotation.

- $\Psi_c$ , the corotation critical argument.
- The eccentricity vector,  $\vec{e} = (h, k)$ , where  $h = e \cdot \cos(\Psi_1)$  and  $k = e \cdot \sin(\Psi_1)$ .

The equations are derived under the following assumptions:

- The eccentricities and inclinations of the particle and satellite orbits are small, which validates the expansion of  $\langle \Phi_s \rangle$ .
- $\xi \ll 1$ , this assumption allows one to expand the potential around the corotation radius  $a_0$ .
- $\sqrt{\varepsilon} = \sqrt{M_s/M_p} \ll 1$ , which simplifies the expression of  $\dot{\Psi}_c$ . When this assumption breaks down, new terms enter in  $\dot{\Psi}_c$ . In particular, these terms eventually destabilize the Lagrange points  $L_4$  and  $L_5$  for sufficiently high values of  $\varepsilon$ .
- Only the horizontal motion of the particle is studied here. In particular, we assume that in case (3) (inclined satellite), the vertical motion of the particle is decoupled from its horizontal motion. This can be shown to be valid as long as the inclination of the particle's orbit is negligible with respect to that of the satellite:  $i \ll i_s$ . Furthermore, the eccentricity of the particle orbit is assumed to be much smaller than that of the satellite orbit,  $e \ll e_s$ , which simplifies also the equations of motion.

Under these assumptions, we obtain the following equations of motion, near a corotation resonance perturbed by a Lindblad resonance.

*Case (1).* The particle shares the orbit of satellite  $S$  and is at the outer Lindblad resonance  $m : m + 1$  with satellite

$S'$  (Fig. 3a). Let  $\Delta n_s = (m + 1)n'_s - mn_s$  be the distance, in frequency, of satellite  $S'$  to exact commensurability with satellite  $S$ . The corotation radius  $a_0$  is then defined by

$$\frac{n_s}{n_0} = 1 + 3 \left( \frac{R_p}{a_0} \right)^2 J_2 - \varepsilon' \beta_0'^2 \frac{db_{1/2}^{(0)}}{d\beta}, \quad (5)$$

where  $a_0^3 n_0^2 = GM_p$  and  $\beta_0' = a_0/a'_s$ . Because  $J_2$  and  $\varepsilon'$  are small quantities,  $a_0$  is close to  $a_s$ . Then:

$$\begin{aligned} \dot{\xi}/n_0 &= -2\varepsilon(df/d\Psi_c) - [2m\varepsilon'\beta_0'A'.k] \\ \dot{\Psi}_c/n_0 &= -3\xi/2 \\ \dot{h}/n_0 &= -\{[3m\xi/2] + \Delta n_s/n_0\}.k \\ \dot{k}/n_0 &= \{[3m\xi/2] + \Delta n_s/n_0\}.h + \varepsilon'\beta_0'A'. \end{aligned} \quad (6)$$

where dots stand for time derivative and  $f(\Psi_c) = \cos(\Psi_c) - 1/[2\sin(\Psi_c/2)]$ .

These four equations form a closed system which completely describes the evolution of the particle resonant variables  $\xi$ ,  $\Psi_c$ ,  $h$ , and  $k$ . An important aspect of these equations is that they show how the *coupling* between the two resonances occurs. As stated in Section 2.3, this is this coupling which must be explicitied in order to address the question of the arc stability. The coupling terms are bracketed in Eqs. (6). When these terms are dropped, the motion of the particle can be split into two simple one-degree of freedom motions: a pendulum-like motion describing the evolution of  $\xi$  and  $\Psi_c$ , under the influence of the corotation resonance (first two equations) and a harmonic motion describing the evolution of  $h$  and  $k$ , under the influence of the Lindblad resonance (last two equations).

More precisely, without the bracketed terms, the first two equations yield

$$\begin{aligned} \ddot{\Psi}_c &= 3\varepsilon n_0^2 (df/d\Psi_c) \\ \dot{\xi} &= -2\dot{\Psi}_c/(3n_0), \end{aligned} \quad (7)$$

which describes the pendulum-like motion of a particle in the potential  $-3\varepsilon n_0^2 f$ , i.e., stable oscillations near the minima of  $-f$  (Lagrange points  $L_4$  and  $L_5$  at  $\Psi_c = \pi/3$  and  $2\pi/3$ , respectively), and unstable motion near the maximum of  $-f$  at  $\Psi_c = \pi$  (Lagrange point  $L_3$ ). Because  $\xi \propto \dot{\Psi}_c$ , the physical motion of the particle guiding center  $[\xi(t), \Psi_c(t)]$  in the corotating frame mimics the motion of a simple pendulum  $[\Psi_c(t), \dot{\Psi}_c(t)]$  in the phase space. This motion is classically divided into librating motion around

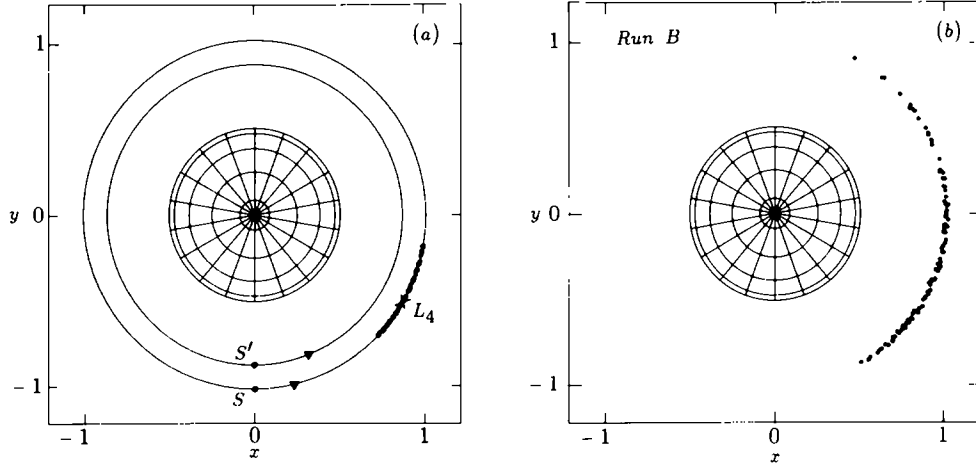


FIG. 3. (a) Typical initial conditions: the 100 particles are initially near the  $L_4$  Lagrange point of a satellite  $S$ , and are resonantly perturbed by a satellite  $S'$  (outer Lindblad resonance 4:5). For sake of clarity, in these plots and those followings, the particles are drawn bigger than they actually are. (b) Run B: effect of inelastic collisions on the stability of the  $L_4$  point. The mass of satellite  $S$  is  $10^{-4}$ , while  $S'$  has a zero mass. The radius of the particles is  $\rho = 10^{-3}$ . The system is shown after 317 revolutions and 341 collisions. The azimuthal spreading is evident by comparison with (a).

$L_4$  and  $L_5$ , and circulating motions beyond the separatrix which passes through the saddle point  $L_3$  (Fig. 1b). The typical oscillation frequency of  $\Psi_c$  near the maximum of  $f$  is given by  $\sqrt{3\varepsilon|d^2f/d\Psi_c^2|}$ , i.e.,  $\sqrt{27\varepsilon/4}$  near  $\Psi_c = \pi/3$  and  $2\pi/3$ .

Dropping again the bracketed terms, the last two equations of (6) yield:

$$\begin{aligned} \ddot{h} &= -(\Delta n_s)^2(h - e_0) \\ \ddot{k} &= -(\Delta n_s)^2k, \end{aligned} \quad (8)$$

where the forced eccentricity  $e_0$  is  $e_0 = \varepsilon'\beta'_0 A n_0 / \Delta n_s$ . These two equations describe the harmonic motion of  $h$  and  $k$  around  $e_0$  and 0, respectively. Again, since  $\dot{h} \propto k$ , the motion of the eccentricity vector  $[h(t), k(t)]$  mimics the trajectory  $[h(t), \dot{h}(t)]$  of a harmonic oscillator in the phase space. These trajectories are a family of circles centered around the forced eccentricity  $(e_0, 0)$ . These circles are swept at the same angular velocity  $\Delta n_s$ .

As is apparent from the equations below, the remaining cases (2) and (3) yield dynamical behaviors very similar to that of case (1).

*Case (2).* The particle is at a corotation resonance  $m : m + 1$  with a satellite whose orbit is eccentric (Fig. 1c). The reference radius  $a_0$  is now defined by

$$\frac{n_s}{n_0} = \frac{m}{m+1} \cdot \left[ 1 + \frac{\dot{\omega}_s}{mn_0} + 3 \left( \frac{R_p}{a_0} \right)^2 J_2 - \varepsilon\beta_0^2 \frac{db^{(0)}/d\beta} \right]. \quad (9)$$

Again,  $\varepsilon$ ,  $J_2$ , and  $\dot{\omega}_s$  are small quantities, so that  $a_0$  is close to  $(m/m+1)^{2/3} a_s$ . The equations of motion are now

$$\begin{aligned} \dot{\xi}/n_0 &= -2m\varepsilon\beta_0 \{ E e_s \cdot \sin(\Psi_c) + [A \cdot k] \} \\ \dot{\Psi}_c/n_0 &= 3m\xi/2 \\ \dot{h}/n_0 &= -\{ [3m\xi/2] + \dot{\omega}_s/n_0 \} \cdot k \\ \dot{k}/n_0 &= \{ [3m\xi/2] + \dot{\omega}_s/n_0 \} \cdot h + \varepsilon\beta_0 A. \end{aligned} \quad (10)$$

As before, the bracketed terms describe the coupling between the corotation and the Lindblad resonances.

*Case (3).* The particle is at a corotation resonance  $m : m + 1$  with a satellite whose orbit is inclined (Fig. 1d). The reference radius  $a_0$  is now defined by:

$$\frac{n_s}{n_0} = \frac{m}{m+1} \left[ 1 + \frac{\dot{\Omega}_s}{mn_0} + 3 \left( \frac{R_p}{a_0} \right)^2 J_2 - \varepsilon\beta_0^2 \frac{db^{(0)}/d\beta} \right], \quad (11)$$

so that  $a_0 \sim (m/m+1)^{2/3} a_s$ . Furthermore,

$$\begin{aligned} \dot{\xi}/n_0 &= 2m\varepsilon\beta_0 \{ 2i_s^2 V \cdot \sin(\Psi_c) - [A \cdot k] \} \\ \dot{\Psi}_c/n_0 &= 3m\xi/2 \\ \dot{h}/n_0 &= -\{ [3m\xi/2] + \dot{\Omega}_s/n_0 \} \cdot k \\ \dot{k}/n_0 &= \{ [3m\xi/2] + \dot{\Omega}_s/n_0 \} \cdot h + \varepsilon\beta_0 A. \end{aligned} \quad (12)$$

The forced eccentricity  $e_0$  of the particle in each of these cases is obtained by setting all the time derivatives to zero; thus,

$$\begin{aligned} \text{case(1): } e_0 &= -\varepsilon' n_0 \beta'_0 A / \Delta n_s \\ \text{case(2): } e_0 &= -\varepsilon n_0 \beta_0 A / \dot{\omega}_s \\ \text{case(3): } e_0 &= -\varepsilon n_0 \beta_0 A / \dot{\Omega}_s, \end{aligned} \quad (13)$$

At the exact Lindblad resonance ( $\Delta n_s = 0$ ,  $\dot{\omega}_s = 0$ , or  $\dot{\Omega}_s = 0$ ),  $e_0$  diverges, but then the condition of small eccentricity no longer holds. In any case, collective effects like pressure, viscosity, or self-gravitation, usually prevent such an outcome in typical planetary rings.

### 3.3. Energy and Angular Momentum Transfer

The eventual fate of the arc crucially depends on how the coupling occurs, i.e., on how energy is transferred from the Lindblad resonance to the corotation resonance. We first note that the energy  $\mathcal{E}$  of the test particle, of mass  $M_T$ , in the corotating frame  $R'$  can be split in two parts, one corresponding to the pendulum-like motion,  $\mathcal{E}_c$ , and one corresponding to the harmonic motion,  $\mathcal{E}_1$ , so that  $\mathcal{E} = \mathcal{E}_c + \mathcal{E}_1$ , with  $\mathcal{E}_1/n^2 a^2 M_T = 1/2 e^2$  and

$$\begin{aligned}\dot{\mathcal{E}}_c/n^2 a^2 M_T &= -\frac{3}{2}\xi^2 + \varepsilon f(\Psi_c) \\ \dot{\mathcal{E}}_1/n^2 a^2 M_T &= -\frac{3}{2}\xi^2 + \varepsilon \beta E e_c \cos(\Psi_c) \\ \dot{\mathcal{E}}_c/n^2 a^2 M_T &= -\frac{3}{2}\xi^2 - \varepsilon \beta V i_c^2 \cos(\Psi_c)\end{aligned}\quad (14)$$

in cases (1), (2), and (3), respectively, where the subscript 0 in  $n$ ,  $a$ , and  $\beta$  has been dropped for sake of clarity.

From Eq. (3), we have  $\dot{\mathcal{E}} = \dot{\mathcal{E}}_c + \dot{\mathcal{E}}_1 = (n_s - n)\Gamma$ , where  $\Gamma$  is the torque exerted, in an inertial frame, by the satellite responsible for the Lindblad resonance on the test particle  $T$ . Near the  $m:m+1$  resonance, we have  $n_s - n \sim -n/(m+1)$ . Furthermore, from Eqs. (6), (8), and (10), we obtain the rates of change of  $\mathcal{E}_c$  and  $\mathcal{E}_1$  as functions of  $k$  and  $\xi$ . The resulting equations are similar in the three cases:

$$\begin{aligned}\dot{\mathcal{E}}_c + \dot{\mathcal{E}}_1 &= -n\Gamma/(m+1) \\ \dot{\mathcal{E}}_c/n^3 a^2 M_T &= \frac{3}{2}m\xi(\varepsilon\beta Ak) \\ \dot{\mathcal{E}}_1/n^3 a^2 M_T &= \varepsilon\beta Ak.\end{aligned}\quad (15)$$

These are the basic equations which tell us how the total energy  $\mathcal{E} = \mathcal{E}_c + \mathcal{E}_1$  of the particle, in the corotating frame, is changed by the Lindblad resonance through the torque  $\Gamma$ , and how it is then transferred to the corotation resonance. Note that the last two equations of this system yield  $\dot{\mathcal{E}}_c/\dot{\mathcal{E}}_1 = O(\xi) \ll 1$ . For instance, in a typical Neptunian arc of width  $< \sim 15$  km, orbiting at  $\sim 60,000$  km from the planet, we have  $\xi < \sim 2 \times 10^{-4}$ . Consequently, most of the energy provided by the satellite is used to increase the eccentricity of the particles, *not* to confine the particles around the potential maximum due to the corotation. Thus stabilizing an arc requires that the total energy provided by the satellite be transferred in potential energy, allowing the guiding centers of the particles to "climb up" the potential hill created by the corotation. As we see

now, this transfer depends on the interactions between the particles.

### 3.4. Effect of Particle Interactions

By first neglecting  $\dot{\mathcal{E}}_c$  in the first equation of the system (15), we obtain

$$\Gamma/n^2 a^2 M_T = -(m+1)\varepsilon\beta Ak, \quad (16)$$

which has a straightforward physical interpretation: it expresses that the torque exerted by the satellite is proportional to  $k = e_c \sin(\Psi_1)$ . This is because the torque exerted on a given particle orbit is proportional to the deformation of the orbit, i.e.,  $e$ , and is also proportional to the sine of the phase lag between the satellite and the orbit, i.e.,  $\sin(\Psi_1)$ , see Fig. 2b. Note also from Fig. 2b that the torque exerted on the streamline has the *opposite* sign of  $k$ . This is confirmed by Eq. (16), since  $(m+1)A$  is always positive.

Substituting  $k$  as a function of  $\Gamma$  in the second equation of the system (15) then yields

$$\dot{\mathcal{E}}_c = -\frac{3}{2}n_c \xi \Gamma. \quad (17)$$

The long-term stability of the particle around the corotation radius depends on the average value of  $\dot{\mathcal{E}}_c$ , which must be positive to counteract the dissipative effect of collisions. More precisely, one must estimate the integral of  $\xi\Gamma$  along a complete libration period  $T_c$  of the particle around the corotation equilibrium point. Two simplifications allow one to make this estimation: (1) the corotation variable  $\xi$  is actually little affected by the nearby Lindblad resonance, for cases of interest around Neptune and (2)  $\xi$  varies sufficiently slowly that at each moment  $h$  and  $k$  have the quasi-stationary values they would have if  $\xi$  were constant.

To justify the first simplification, consider for instance the case (3), where we compare the terms  $2i_c^2 V$  and  $A.k$  in Eq. the first equation of Eqs. (12). As we shall see in Section 4, the term  $2i_c^2 V$  is related to the maximum amplitude  $\xi_m$  of the radial excursion of the guiding center by  $2i_c^2 V = 3\xi_m^2/(8\beta\varepsilon)$ . The actual width  $w$  of the arc must be less than  $2a_0\xi_m$  for the latter to be azimuthally confined, thus  $2i_c^2 V > \sim 3(w/a_0)^2/(32\beta\varepsilon)$ . For a typical width and radius of the arc  $w \sim 15$  km,  $a_0 \sim 60,000$  km, and a typical mass of the satellite  $\varepsilon \sim 10^{-9}$ , this yields  $2i_c^2 V > \sim 6$ . On the other hand,  $A \sim m$ , so that  $|Ak| \sim \varepsilon m \ll 2i_c^2 V$ , thus the corotation resonance is little affected by the Lindblad resonance. Consequently,  $\xi$  has a pendulum-like motion described by the first two equations in Eqs. (12), where the bracketed term  $A.k$  can be dropped.

To justify the second approximation, we note that the typical oscillation frequency for  $\xi$  is  $n_c \sim n\sqrt{6m^2 i_c^2 V \varepsilon \beta_0}$

$\sim mn\sqrt{6\beta_0}(w/a_0)$ , so that  $n_c \leq 3 \times 10^{-3}n$  with the previous numerical values. The typical time for two nearby streamlines to reach a steady state under the effect of collisions and under the effect of the Lindblad resonance, is the time between two collisions for a given particle, i.e., a few revolutions around the planet. Thus, the time scale for variation of  $\xi$  is sufficiently large compared to the revolution period, that  $h$  and  $k$  may be considered as constant, depending only on the instantaneous value of  $\xi$ . In conclusion, we have to calculate the integral of  $\xi(t)\Gamma(\xi)$  along a libration period, where  $\xi(t)$  is a known function of time, and  $\Gamma$  is a known function of  $\xi$ .

Up to now, we have been concerned only by the evolution of a *single* test particle. It may be more convenient to rewrite Eq. (17) per unit mass of the arc. Let  $\Sigma_0$  be the unperturbed surface density of the arc, so that the mass of an annulus of radius  $a$  and width  $da = a d\xi$  is  $dM = 2\pi\Sigma_0 a^2 d\xi$ . Then, the rate of change of energy  $d\dot{\mathcal{E}}_c$  of this annulus, at the radius  $a$  is

$$d\dot{\mathcal{E}}_c dM = - \left( 3n_c \xi \frac{d\Gamma}{d\xi} \right) / (4\pi a^2 \Sigma_0), \quad (18)$$

where  $d\Gamma/d\xi$  is the *torque density*, i.e., the torque exerted by the satellite per unit radius, or per streamline. Finally, if  $M_A$  denotes the total mass of the arc, the rate of change per unit mass  $\langle \dot{\mathcal{E}}_c \rangle / M_A$ , averaged over one libration period  $T_c$  of all the particles around the corotation point is

$$\langle \dot{\mathcal{E}}_c \rangle / M_A = - \frac{3}{4\pi} \cdot \frac{n_s}{a^2 \Sigma_0} \cdot \frac{1}{T_c} \int_{T_c} \xi \frac{d\Gamma}{d\xi} dt. \quad (19)$$

This constitutes the basic equation which tells us where, and how much, energy is deposited by the satellite to the guiding centers of the particles, in the different places of the arc. One must note that Eq. (19) is very general, and is valid in particular whether the torque density varies rapidly or not inside the arc, and also whether the resonances are isolated or overlapping near the arc.

Because of the presence of the term  $\xi$  in front of  $d\Gamma/d\xi$  in the integrand, the energy received by the guiding centers is not proportional to the total torque  $\Gamma$ , but rather, to the *gradient* of the torque density, i.e.,  $d^2\Gamma/d\xi^2$ . Physically, this means that a given particle must receive more angular momentum on the inner side of its libration path than on the outer side, in order to compensate for the spreading effect due to dissipation.

The next step is to determine the function  $d\Gamma/d\xi$  as a function of  $\xi$  near a resonance, or near a set of overlapping resonances. The effect of a Lindblad resonance is to disturb the streamlines near the resonance radius. Because of the interactions between the particles, this disturbance propagates away from the resonance. Depending on the

kind of interactions (pressure, viscosity, self-gravitation, collisions, gas drag, . . .), the disturbance may propagate as a wave, or may die off if the dissipative effects are dominant. The torque density  $d\Gamma/d\xi$  mimics the behavior of the disturbance, i.e., damps if dissipation is dominant and oscillates if a spiral wave is launched (Goldreich and Tremaine 1982, Meyer-Vernet and Sicardy 1987). The values of the *total* torque  $\Gamma = \int (d\Gamma/d\xi) d\xi$ , integrated over the resonance width, is largely independent not only of the numerical values of the disk parameters (density, pressure, viscosity, drag coefficient), but also of the very physical process at work in the disk (Ibid.). However, since the value of  $\dot{\mathcal{E}}_c$  depends on the torque density gradient, the stability of the arc depends on the particular behavior of the disturbance near the Lindblad resonance.

The general shape of the torque density  $d\Gamma/d\xi$ , near an isolated Lindblad resonance, is usually a bell-shaped function peaking at the resonance radius, with a possible wavy behavior if the damping is not too important (see Figs. 1, 2, 5–7 of Meyer-Vernet and Sicardy 1987). Furthermore, the torque density peak is positive if the resonance is outside the satellite (outer Lindblad resonance) and negative if it is inside (inner Lindblad resonance); i.e., the torque tends to push the particles away from the satellite. Consequently the gradient of torque density tends to be negative (positive) just outside an outer (inner) Lindblad resonance, and positive (negative) just inside. Thus, to be trapped, an arc should stay just outside (inside) the outer (inner) Lindblad resonance radius. This conclusion was first derived, and numerically tested, by Lin, Papaloizou, and Ruden (1987) in the case where the interactions between particles are modeled as an exponential decay of the particle orbital eccentricities. A similar conclusion is derived in the case where the Lindblad resonances overlap (Lissauer 1985). In this case, the torque density is uniformly decreasing function of radius, independent of the fact that the shepherding satellite is inside or outside the arc, which ensures the confinement of the arc in both cases.

It should be emphasized, however, that for an isolated resonance, the torque density may have a wavy behavior. Furthermore, the arc may have a width smaller than the resonance width. Thus the gradient of the torque density may have some complicated variations. In this case, it not obvious whether the arc should stay outside or inside the corotation radius. Rather, one must then go back to Eq. (19), and then perform the integration of  $\xi(d\Gamma/d\xi)$  for each case of interest.

### 3.5. The Energy–Eccentricity Diagram

For interpreting more readily the results of the numerical simulation, we use a  $(\mathcal{E}, \mathcal{E}_1)$  diagram, where the value of  $\mathcal{E}_1$ , i.e., essentially the square of eccentricity of a parti-

cle, is plotted against the total energy  $\mathcal{E} = \mathcal{E}_c + \mathcal{E}_1$  in the corotating frame  $R'$ . We call these diagrams "energy–eccentricity" diagrams, and they show how much energy is dissipated in the arc (decrease of  $\mathcal{E}$ ) and how eccentricity is pumped up by the Lindblad resonance (increase of  $\mathcal{E}_1$ ).

For sake of conciseness, we use dimensionless units for the plots. The origin of the energy  $\mathcal{E}$ , denoted  $\mathcal{E}_0$ , is taken as the energy of a particle at rest at the maximum of the corotation potential. The unit of energy for  $\mathcal{E}$  is the difference  $\Delta\mathcal{E}$  between the potential maximum and the potential at the saddle points (see Eqs. (14)):

$$\begin{aligned}\mathcal{E}_0 &= -\frac{1}{2}n^2a^2\varepsilon\beta M_T & \Delta\mathcal{E} &= n^2a^2\varepsilon\beta M_T \\ \mathcal{E}_0 &= n^2a^2\varepsilon\beta e_\surd |E| M_T & \Delta\mathcal{E} &= 2n^2a^2\varepsilon\beta e_\surd |E| M_T \\ \mathcal{E}_0 &= n^2a^2\varepsilon\beta i_\surd^2 |V| M_T & \Delta\mathcal{E} &= 2n^2a^2\varepsilon\beta i_\surd^2 |V| M_T,\end{aligned}\quad (20)$$

in cases (1), (2), and (3), respectively.

Furthermore, the energy unit for  $\mathcal{E}_1$  will be taken equal to  $n^2a^2M_T\beta\varepsilon$ . This value corresponds to the typical eccentricity that a particle should have to explore the libration corotation region. The quantities plotted in the energy–eccentricity diagrams are thus

$$\begin{aligned}\mathcal{E}' &= (\mathcal{E} - \mathcal{E}_0)/\Delta\mathcal{E} \\ \mathcal{E}'_1 &= \mathcal{E}_1/[n^2a^2\beta\varepsilon M_T].\end{aligned}\quad (21)$$

The  $(\mathcal{E}', \mathcal{E}'_1)$  diagram is then divided in three regions (Fig. 5):

- *A forbidden region.* Since  $\mathcal{E}'_1 \propto e^2$ ,  $\mathcal{E}'_1 < 0$  defines a first forbidden region. Furthermore, because  $\mathcal{E}'_c \leq \mathcal{E}_0$ , one must have

$$\mathcal{E}'_1 \geq \frac{\Delta\mathcal{E}}{n^2a^2\beta\varepsilon M_T} \mathcal{E}', \quad (22)$$

which defines a second forbidden region, below the line  $\mathcal{E}'_1 = s\mathcal{E}'$ , where the slope  $s$  is given by

$$\begin{aligned}s &= 1 \\ s &= 2e_\surd |E| \\ s &= 2i_\surd^2 |V|\end{aligned}\quad (23)$$

in the cases (1), (2), and (3), respectively.

- *A libration region.* If  $\mathcal{E}_0 - \Delta\mathcal{E} \leq \mathcal{E}'_c \leq \mathcal{E}_0$ , the corotation critical argument  $\Psi_c$  is trapped in libration. This condition is equivalent to

$$s\mathcal{E}' \leq \mathcal{E}'_1 \leq s(\mathcal{E}' + 1). \quad (24)$$

The libration region is confined between two parallel

lines of slope  $s$ , one of which defining the forbidden region (Fig. 5).

- *A circulation region.* If  $\mathcal{E}'_1 \geq s(\mathcal{E}' + 1)$ ,  $\Psi_c$  circulates and the particle no longer belongs to the arc.

Dissipation of energy due to collisions decreases the energy  $\mathcal{E}'$ , thus pulling the particles in the arc toward the separatrix. As we saw before, the energy provided by the satellite tends essentially to increase  $\mathcal{E}'_1$ , while little affecting  $\mathcal{E}'_c$  (Eqs. (15)). Thus the Lindblad resonance tends to move the particles parallel to the inclined lines in the energy–eccentricity diagram (see, for instance, Fig. 12b).

#### 4. ORDER OF MAGNITUDE CONSIDERATIONS

The aim of our simulation is to describe a dynamical system which, hopefully, has the same qualitative behavior as the system we want to study. Then, scaling factors should allow us to apply the results obtained in the simulation to real systems. The three basic ingredients which must be common to the simulation and real arcs are: (1) inelastic collisions between finite-size particles, (2) a maximum of potential energy created by a corotation resonance, and (3) a nearby Lindblad resonance. The corresponding parameters are: the particle size, the mass of the satellite responsible for the corotation resonance, and the mass of the satellite responsible for the Lindblad resonance (which may be the same satellite, see above).

We shall see in the next section that the typical satellite masses used in the simulation are in the range  $\varepsilon \sim 10^{-5} - 10^{-4}$ , while the typical particle sizes are  $\sim 10^{-3}$ , i.e., about 50 km when scaled to Neptune's size. As we see, this does not correspond, by far, to real parameters: for instance, the small newly discovered Neptune's satellites have masses in the range  $\varepsilon \sim 10^{-9} - 3 \times 10^{-7}$  (Smith *et al.* 1989), while the arc contains billions of small particles, not hundred big particles. From a computational point of view, however, the requirement is that significant effects appear after a reasonable consumption time. In particular, the number of particles cannot be too large, the dissipation of energy through collisions must be large enough, and the balancing energy from the satellite must be correspondingly large. This section is thus intended to give a few order of magnitude calculations which may be useful (1) for estimating typical time scales of evolution in real arcs, (2) for connecting these time scales to those of the numerical code, and finally, (3) for determining a reasonable sets of the parameters to be entered in the runs.

*Particle size and optical depth.* The finite size of the particles is important, since it causes nearby particles on different orbits to collide, thus dissipating energy while conserving angular momentum, and eventually leading to the spreading of narrow rings (Brahic 1977, Brahic and

Hénon 1977). The time scale for this spreading is directly linked to the collision frequency, i.e., the optical depth. The optical depth  $\tau$  of an arc of length  $L$  and width  $w$ , and composed of  $N$  particles with radius  $\rho$  is

$$\tau \sim \frac{N\rho^2}{wL}, \quad (25)$$

which shows that the collisional evolution time of the system scales like  $N\rho^2$ ; in other words, a few hundred big particles can represent the evolution of many small particles (Brahic 1976).

*Width of the corotation resonance.* The maximum width of the region where the guiding centers of the particles are trapped in libration motion, due to the corotation resonance, is directly linked to the mass of the satellite causing the resonance. We derive here the value of this width in the case of a satellite with an inclined orbit, the other cases being treated in very much the same way. The energy  $\mathcal{E}_c$  associated with the corotation resonance is proportional to  $-(3/8)\xi^2 - \varepsilon\beta Vi_s^2 \cos(\Psi_c)$  (Eq. (14c)), which is thus conserved if we neglect the perturbations due to the Lindblad resonance. The maximum radial excursion  $\xi_m$  of a particle is reached on the separatrix between libration and circulation motions (Fig. 1d). The saddle points correspond to  $\Psi_c = 0$  and  $\xi = 0$ , so that along the separatrix, we have  $-(3/8)\xi^2 - \varepsilon\beta Vi_s^2 \cos(\Psi_c) = -\varepsilon\beta Vi_s^2$ . The maximum radial excursion  $\xi_m$  is thus reached for  $\Psi_c = \pi$ , which yields  $2i_s^2 V = 3\xi_m^2/(8\beta\varepsilon)$ .

*Strength of the corotation resonance.* Equations (14) show that the difference of potential energy (per unit mass) between the stable corotation point and the unstable saddle point is

$$\Delta\mathcal{E}_c/M_T \sim \varepsilon n^2 a^2, \quad (26)$$

with additional factors of order  $e_s$  and  $i_s^2$  in the right-hand side of the equation in cases (2) and (3), respectively. On the other hand, the energy dissipated per particle, per revolution, and per unit mass, is

$$\Delta\mathcal{E}_d/M_T \sim c^2 \frac{\tau}{T_{\text{orb}}}, \quad (27)$$

where  $T_{\text{orb}}$  is the period of revolution and  $c$  is the velocity dispersion in the arc, i.e., also the typical relative velocity of two colliding particles. This equation assumes that a substantial amount of the relative kinetic energy of the particles is lost during the collision. We assume also that  $c$  is maintained by the Keplerian differential motion, i.e.,  $c \sim \rho n$ . Thus, the typical time for a particle to fall down from the stable corotation point to the unstable saddle point is

$$t_{\text{spread}} = \frac{\Delta\mathcal{E}_c}{\Delta\mathcal{E}_d} \sim \varepsilon \left(\frac{a}{\rho}\right)^2 \frac{T_{\text{orb}}}{\tau} \quad (28)$$

which is the typical time for an arc to be destroyed by inelastic collisions. This timescale must be multiplied by factors of order  $e_s$  and  $i_s^2$  in cases (2) and (3), respectively. Note also that the spreading time scales like  $\varepsilon/\rho^2$ .

*Strength of the Lindblad resonance.* For the arc to be stable, the energy  $\langle\dot{\mathcal{E}}_c\rangle$  provided to the guiding centers of the particles should be comparable to the dissipation rate due to collisions. The estimation of  $\langle\dot{\mathcal{E}}_c\rangle$  is, however, rather difficult because it depends on the particular physics of particles interactions (see Eq. (19) and the subsequent discussion).

A crude estimate of  $\langle\dot{\mathcal{E}}_c\rangle$  may be nevertheless derived as follows. First we note that the gradient of torque density, normalized to the total torque  $\Gamma_m$  exerted by the satellite at the  $m:m+1$  resonance, may be written under the form:

$$(d\Gamma/d\xi)/\Gamma_m = g(\xi), \quad (29)$$

where  $g(\xi)$  is a dimensionless function whose integral is equal to unity. The function  $g$  reaches a maximum value of  $1/\alpha$  at the resonance ( $\xi = 0$ ), and decays over a typical distance of  $\xi \sim \alpha$  on each side of the resonance. Thus, the typical value of the derivative of  $g$  near the resonance is  $dg/d\xi \sim 1/\alpha^2$ . The dimensionless coefficient  $\alpha$  describing the behavior of  $g$  takes into account the physics at work in the arc, and is a function of various parameters like the viscosity coefficients, the velocity dispersion, and the disk surface density (see Table I of Meyer-Vernet and Sicardy 1987).

We use, on the other hand, the standard torque formula  $\Gamma_m = \mathcal{F}_m m^2 \Sigma_0 a_s^4 n_s^2 \varepsilon'^2$ , where the number  $\mathcal{F}_m$  is a slowly varying function of  $m$ , which tends toward  $\sim 8.5$  for large  $m$  (Goldreich and Tremaine 1982). Combining this result with Eqs. (17) and (29) yields the instantaneous value of  $\dot{\mathcal{E}}_c$  per unit mass:

$$\dot{\mathcal{E}}_c/M_A \sim 3\mathcal{F}_m m^2 a_s^3 n_s^2 \varepsilon'^2 \xi g(\xi)/4\pi. \quad (30)$$

The average value of  $\xi g(\xi)$  during one libration period of a particle in the corotation potential may be estimated by expanding  $g$  to first order around  $\xi = 0$  and by noting that the variation of  $\xi$  with time is approximately harmonic; thus,

$$\langle\xi g(\xi)\rangle \sim \frac{\xi_m^2}{2} \frac{dg}{d\xi}, \quad (31)$$

where  $\xi_m$  is the radial amplitude of the libration motion of

the particle, i.e., the half width of the arc. From  $dg/d\xi \sim \alpha^2$ , we finally obtains

$$\langle \dot{\xi}_d \rangle / M_A \sim 3\mathcal{F}_m m^2 a^2 n^3 \varepsilon'^2 \xi_m^2 \alpha^2 / 8\pi. \quad (32)$$

As seen before, the typical dissipation rate per unit mass due to collisions is  $\dot{\xi}_d / M_A \sim \tau c^2 n / 2\pi \sim \tau \rho^2 n^3 / 2\pi$ . Thus, we have  $\dot{\xi}_c \sim \dot{\xi}_d$  for

$$\varepsilon' \sim \sqrt{\frac{4\tau}{3\mathcal{F}_m}} \cdot \frac{\rho}{ma_s \xi_m} \alpha. \quad (33)$$

The last parameter to be estimated is now  $\alpha$ . The arc that we simulate is dominated by collisions, i.e., pressure and viscosity, with no self-gravitation, so that  $\alpha$  is given by (Meyer-Vernet and Sicardy 1987):

$$\alpha \sim \frac{1}{3m} \left( \frac{c}{an} \right)^2 \sim \frac{1}{3m} \left( \frac{\rho}{a} \right)^2. \quad (34)$$

## 5. NUMERICAL SIMULATION

### 5.1. The Code

The code used here is an extension of a code initially developed by Brahic (1976) to study the flattening and the radial spreading of a collisional disks (Brahic 1977, Brahic and Hénon 1977). This code has been modified to take into account the disturbing effect of small satellites, with arbitrary eccentricities and inclinations (Sicardy 1988, 1991). The main characteristics of the code are the following:

- The code calculates the 3-D motion of  $N = 100$  particles orbiting a massive central body (the planet). Each particle is followed step by step in a deterministic way.
- The only interactions between particles are inelastic collisions. Self-gravitation, radiation drag, and plasma drag are ignored.
- The particles are identical hard spheres which suffer instantaneous collisions. No accretion or fragmentation occurs. The relative velocity  $\vec{V}_{rel}$  of two particles just before a collision is split into two components: a radial component  $\vec{V}_r$  which is the projection of  $\vec{V}_{rel}$  along the line joining the center of the particles, and a transverse component  $\vec{V}_t$  perpendicular to  $\vec{V}_r$ . Just after the collision,  $\vec{V}_r$  and  $\vec{V}_t$  are multiplied by the rebound coefficients  $k_r$  and  $k_t$ , with  $-1 \leq k_r \leq 0$  and  $0 \leq k_t \leq 1$ .
- Between two collisions, each particle follows a Keplerian orbit gravitationally perturbed by the satellites. The satellites are not perturbed by the particles and do not interact with each other. The particle orbital elements

are modified according to Gauss' equations of perturbation.

- Units are such that the gravitational constant  $G = 1$ , and the angular velocity on circular orbits of radius unity is equal to unity.

The main advantage of our model is that it is entirely deterministic, with no a priori assumptions regarding the statistics of collisions. The accuracy of the calculation is high: typically the angular momentum is conserved with a relative accuracy of  $5 \times 10^{-7}$  after 1000 collisions (Sicardy 1991), so that small systematic trends like exchange of angular momentum with a satellite may be easily tracked. The main limitation of the code remains, however, the time consumption, typically 8 sec of CPU time per arc revolution on a Cray 1 computer, and about 100 sec on a Sun 4 computer, with  $N = 100$  particles. The runs were achieved on a Cray 1 computer, at the Centre de Calcul Vectoriel pour la Recherche (Palaiseau, France) and on a Sun 4 computer at Cornell University.

### 5.2. Choice of Parameters

The various parameters used in our runs are summarized in Table II. They correspond to a compromise between the mechanisms we want to display and the available computing time. The calculations of Section 4 allow one to estimate these parameters, and to show also how they scale to real parameters.

*Particle size.* In our runs, the particle size has been adjusted so that a given particle undergoes about one collision per revolution, i.e., the optical depth is of order unity. If there are many collisions, then a hydrodynamical approach is more appropriate, and if there are significantly fewer collisions, the dynamical evolution of the system is too slow. For the differential Keplerian motion to be visible in a few revolutions, the width of the arc must be a few times the radius of the particles, i.e.,  $\rho$  must be a few times  $L\tau/N$ , according to Eq. (25). Taking  $L \sim 0.1$  (the initial length of the arc),  $\tau \sim 1$  and  $N = 100$ , this relation requires that  $\rho$  be a few times  $10^{-3}$ .

*Strength of the corotation resonance.* The spreading time of an arc under the effect of inelastic collisions (Eq. (28)) must be small enough so that the spreading be visible during the run, but not too small, so that the resonant satellite has time to provide the energy balancing this dissipation. The typical time between encounters of the resonant satellite and the arc is the sidereal period  $mT_{orb}$ , where  $m$  refers to the  $m : m + 1$  resonance. Taking  $t_{spread} \sim mT_{orb}$ , we obtain

$$\frac{\varepsilon}{\tau} \left( \frac{a}{\rho} \right)^2 \sim m. \quad (35)$$

TABLE II  
Parameters of the Runs

Run	$\varepsilon$	$a_s$	$e_s$	$\dot{\omega}_s$	$\varepsilon'$	$a'_s$	$e'_s$	$\rho$	Coefficient of rebound ( $k_r, k_t$ )	Number of revolutions	Number of collisions
A	0	1	0	0	0	0.86177	0	$10^{-3}$	-0.1, 0.1	160	1,116
B	$10^{-4}$	1	0	0	0	0.86177	0	$10^{-3}$	-0.2, 0.2	318	3,423
C	$10^{-4}$	1	0	0	0	0.86177	0	$2 \times 10^{-3}$	-0.1, 0.1	73	3,240
D	$10^{-4}$	1	0	0	$2 \times 10^{-5}$	0.86177	0	$2 \times 10^{-3}$	-0.1, 0.1	50	4,439
E	$5 \times 10^{-4}$	1	0	0	$2 \times 10^{-4}$	0.86177	0	$10^{-3}$	-0.3, 0.3	30	439
F	$10^{-4}$	1	0	0	$2 \times 10^{-5}$	0.86177	0	$10^{-3}$	-0.2, 0.2	315	13,297
G	$2 \times 10^{-5}$	0.86177	0.1	0	0	0.86177	0	$10^{-3}$	-0.1, 0.1	97	6,393
H	$10^{-4}$	0.86777	0	0	$1.3 \times 10^{-4}$	0.86777	0	$10^{-3}$	-0.2, 0.2	160	1,421
I	$10^{-4}$	0.85557	0	0	$1.3 \times 10^{-4}$	0.85577	0	$10^{-3}$	-0.2, 0.2	160	10,908
J	$7 \times 10^{-5}$	0.86526	0.1	$+3 \times 10^{-2}$	0	0.86177	0	$10^{-3}$	-0.2, 0.2	160	6,904
K	$7 \times 10^{-5}$	0.85836	0.1	$-3 \times 10^{-2}$	0	0.86177	0	$10^{-3}$	-0.2, 0.2	160	8,487

With  $\tau \sim 1$ ,  $a = 1$  and  $\rho \sim 10^{-3}$ , this gives  $\varepsilon \sim 10^{-5}$  used in our runs.

*Strength of the Lindblad resonance.* The mass of the satellite causing the Lindblad resonance is estimated by using Eq. (33). The half width  $\xi_m$  of the arc should be at least a few times the size of the particles. In our runs, we have  $\xi_m \sim 10\rho/a$ , and from  $\tau \sim 1$ ,  $\rho/a \sim 10^{-3}$  and  $m = -5$ , we get

$$\varepsilon' \sim 10^{-5}. \tag{36}$$

With the set of parameters chosen here, the mass of the satellite responsible for the Lindblad resonance is comparable to the mass of the satellite responsible for the corotation resonance. This coincidence allows one to study the cases where there is only one satellite on an eccentric orbit.

We note finally that the exchange of energy at the Lindblad resonance is achieved in our runs through collisions only, i.e., viscosity and acoustic waves. Real rings, however, in regions with typical optical depth of order unity, are dominated by self-gravity rather than viscosity. Nevertheless, the torque formula is sufficiently robust so that it applies to a very wide range of physical processes (Goldreich and Tremaine 1982, Meyer-Vernet and Sicardy 1987). Consequently, the basic dynamics of the arc confinement is conserved in our numerical experiment. Obviously, a more general code taking into account collective effects like self-gravitation would be most interesting, but this is presently beyond the capability of the computers used for this work.

## 6. NUMERICAL RESULTS

### Initial Conditions

Among the various initial conditions used in this work, we will present here four typical configurations:

- A free arc, with no disturbing satellites, which evolves under the effect of collisions only.
- An arc initially confined near the  $L_4$  Lagrange point of a satellite  $S$ .
- An arc initially confined near the  $L_4$  Lagrange point of a satellite  $S$ , and at an isolated Lindblad resonance with a second satellite  $S'$ .
- An arc initially confined near an isolated corotation resonance with a single satellite  $S$ , whose orbit is eccentric.

On the other hand, for these configurations, we have explored two different kinds of dependence: (1) the dependence on physical parameters like the mass of the satellites, the size of the particles, etc., and (2) the influence of the position of the Lindblad resonance with respect to the arc.

Some of our results can be compared to those of Lin, Papaloizou, and Ruden (1987), who use a rather similar code in the great lines, but with significant differences in the details:

- Their code is two-dimensional and semi-deterministic since particles entering in a box of a fixed mesh are given the same velocity relative to their center of mass. This allows them to handle a large number of particles ( $N = 2000$ ).
- The arc is initially widely spread between the  $L_4$  and the  $L_3$  points, and new particles are reintroduced in the system as particles escape through the separatrix. In our runs, the arc is initially well confined around the corotation point, and we study its spreading, or confinement, with no further assumptions as particles escape.
- We study also the stability of an arc at a corotation resonance of a single satellite with an eccentric orbit, which is not done by Lin, Papaloizou, and Ruden.

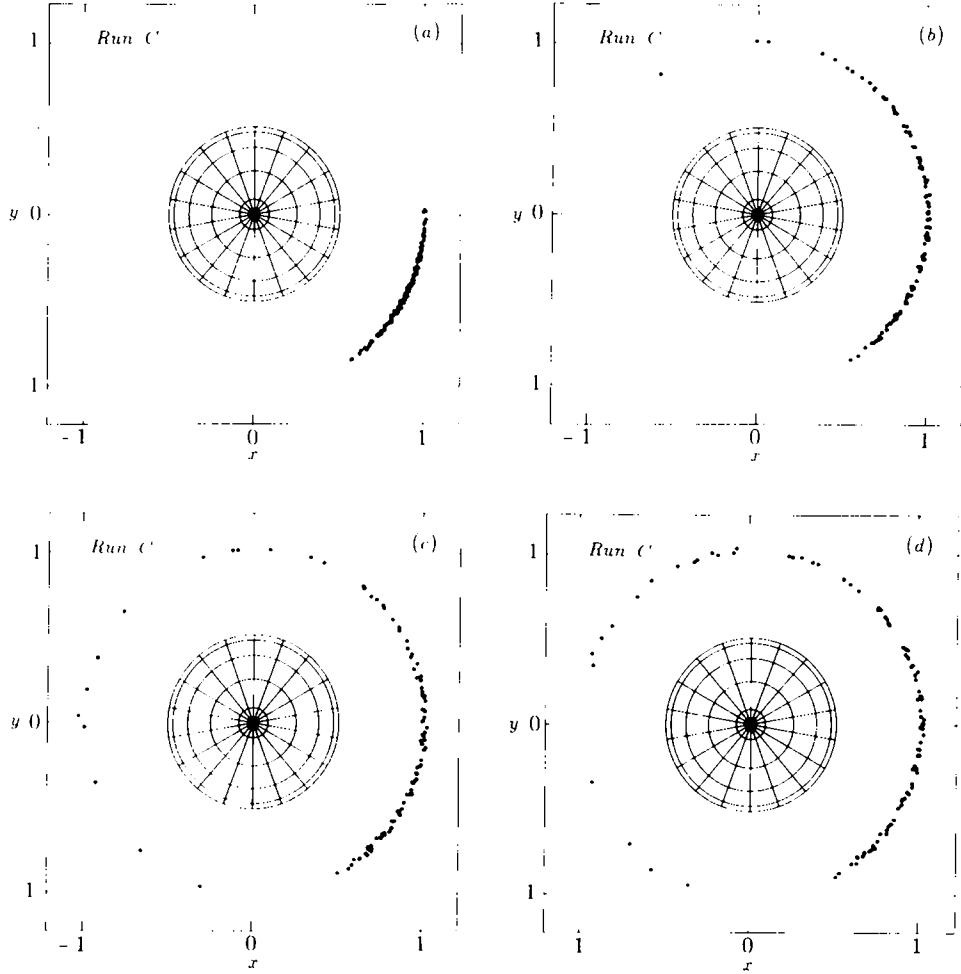


FIG. 4. Run C: the parameters of this run are identical to Run B, except for the particle radius  $\rho = 2 \times 10^{-3}$ . (a) The system after five revolutions and 815 collisions, (b) after 24 revolutions and 1930 collisions, (c) after 47 revolutions and 2737 collisions, and (d) after 73 revolutions and 3240 collisions. The collisions spread the arc on a shorter time scale than in Run B (Fig. 3b).

### 6.1. Free Arc

Typical initial conditions used in several of our runs are shown in Fig. 3a. In Run A considered here, the masses of the satellites have been set to zero. After 40 revolutions and about 15 collisions per particle, the arc has completely spread along the orbit (Fig. 16a). The azimuthal spreading is essentially due to the differential Keplerian motion between the outer and inner edges of the arc of width  $w$ . The spreading time scale is thus:

$$t_{\text{spread}} \sim \frac{2a}{3w} T_{\text{orb}}. \quad (37)$$

With  $a = 1$ ,  $w = 0.01$ , and  $T_{\text{orb}} = 2\pi$ , we have  $t_{\text{spread}} \sim 65$  revolutions, in agreement with the observed spreading time.

### 6.2. Arc near a $L_4$ Point

In the next experiment (Run B), we take the same parameters as for the previous Run A, except that the particles are initially located near the  $L_4$  Lagrange point of a satellite  $S$  of mass  $10^{-4}$ , while the mass of satellite  $S'$  is set to zero. The azimuthal spreading is now much slower than for the previous run. For instance we see that after 317 revolutions and 3411 collisions, i.e., nearly 70 collisions per particle, the arc is still strongly confined near the  $L_4$  point of the satellite  $S$  (Fig. 3b). Everything else equal, the radius of the particles has been doubled in Run C,  $\rho = 0.002$ . The spreading of the arc, shown in Fig. 4, has the same qualitative aspect as in Run B, except that it is now faster.

Contrarily to Run A, the azimuthal spreading in Runs B and C is no longer due to the differential Keplerian motion, but is actually caused by the dissipation of energy

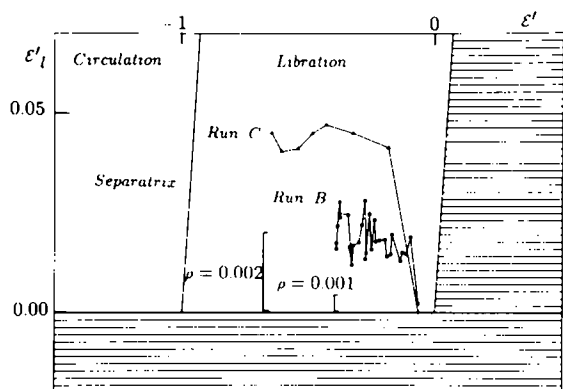


FIG. 5. Evolution of the arc in the "energy-eccentricity" diagram, for Runs B and C. The quantity  $\mathcal{E}'$  is the average energy of a particle in the corotating frame, while  $\mathcal{E}'_1$  is the average energy of a particle stored in the eccentric motion (see Eq. (21)). The hatched region is forbidden, the libration region is enclosed by the forbidden region and the separatrix, and the circulation region is at the left of the separatrix (see Section 3.5). Particles of Run B are half as big as particles of Run C (radius  $10^{-3}$  instead of  $2 \times 10^{-3}$ ), and the collisions are a little less dissipative ( $-k_r = k_t = 0.2$  in Run B and  $-k_r = k_t = 0.1$  in Run C). Otherwise, the parameters are identical (see Table II). After a few collisions, the orbital eccentricity of the particles reaches a finite value, due to their finite size. Collisions dissipate energy and thus drive the particles to the left, toward the separatrix. At the end of each run, the total number of collisions is about the same (3411 for Run B, and 3240 for Run C). The bigger the particles, the bigger the velocity dispersion and the faster the dissipation rate. The vertical bars allow comparison of the average radial excursion of the particles to their own size (see text for details).

due to inelastic collisions. This is apparent when considering the evolution of the arc in the  $(\mathcal{E}', \mathcal{E}'_1)$  diagram (Fig. 5). First, the average value of  $\mathcal{E}'_1$ , or equivalently the mean orbital eccentricity of the particles, rapidly reaches a finite value due to the finite size of the particles. In a second step, the particles move parallel to the  $\mathcal{E}'$  axis toward the separatrix, due to loss of energy. We see in Fig. 5 that the particles in Run C have higher orbital eccentricities and dissipate energy faster. This is because the average dissipation rate due to collisions increases with the velocity dispersion, which in turn increases with the particle size. More precisely, the average eccentricity induced by collisions is such that the random excursion of a particle during one revolution is a few times the size of the particles. This can be checked by considering the vertical bars in Fig. 5, where each bar represents the value of  $\mathcal{E}'_1$  for particles whose radial displacement during one revolution is equal to the particle's diameter. At the end of each run of Fig. 5, the total amount of collisions is about the same (3200–3400), but the energy lost by the bigger particles ( $\rho = 0.002$ ) is about twice the energy lost with the smaller particles ( $\rho = 0.001$ ).

The evolution of the arc in Run C is shown in a  $(\Psi_c, r)$  diagram, where  $\Psi_c = \lambda - \lambda_s$  is the critical corotation

argument, and where  $r$  is the distance to the planet center (Fig. 6). In this diagram, each particle is plotted together with its guiding center. Since the eccentricity of the particles remains small, the particles are at any time very close to their guiding center. Dissipation of energy slowly drives the particles from the potential maximum  $L_4$  to the saddle point  $L_3$ . Some particles have lost enough energy to cross the separatrix and fall on horseshoe orbits.

### 6.3. Arc near a $L_4$ Point, in Resonance with a Second Satellite

In order to balance the energy lost by the arc, a second satellite  $S'$ , called the "shepherd," has been added. Its position is such that the arc lies on the outer Lindblad resonance 4 : 5 of the new satellite (Fig. 3a). Three typical configurations are investigated in this subsection. They correspond to the dividing points between stable and unstable arcs. More precisely, we show here: (1) a case where the mass of the shepherd is too small for balancing the energy dissipated by collisions, so that the arc eventually spreads, (2) a case where the mass of the shepherd is too large, so that the arc receives too much energy and spreads also, and (3) an intermediate case where the arc remains confined.

In the first case of the three examined here (Run D), the parameters are the same as for Run C, except that the second satellite  $S'$  has a mass  $\varepsilon' = 2 \times 10^{-5}$ , instead of zero. The arc now gains energy from  $S'$ , but dissipation is still too important to prevent the arc from spreading. The corresponding arc is shown in Fig. 7a, after 45 revolutions and 4100 collisions, with half a dozen particles already lost on horseshoe orbits. On an energy-eccentricity diagram like that of Fig. 5, we would see the particles moving to the left, slower than in case B, but fast enough to see the arc destroyed during the time of the simulation.

The next case (Run E) shows the opposite trend. Now, the Lagrange satellite has a mass  $\varepsilon = 5 \times 10^{-4}$ , while the shepherd has a mass  $\varepsilon' = 2 \times 10^{-4}$  and the particle radius is  $\rho = 10^{-3}$ . Thus the shepherd is 10 times more massive than in Run D, and the particles are half the size. In other words, the arc receives more energy from  $S'$  and dissipates less energy through collisions. No balance can be reached because the arc cannot dissipate all this energy. Consequently, the eccentricity forced by the Lindblad resonance increases, and the particles cross the separatrix not because they lose energy (leftward motion), but because they increase their value of  $\mathcal{E}'_1$  (upward motion). The destroyed arc is shown in Fig. 7b, after 28 revolutions and 2440 collisions.

In the last case (Run F), we use the same parameters as for Run D, except that the particles are half as big, and the collisions are slightly less dissipative. The energy loss rate is accordingly reduced, which allows the arc to re-

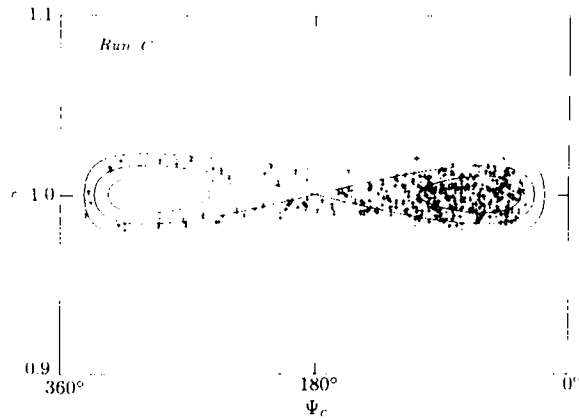


FIG. 6. Run C: the positions of the particles are plotted as dots and their guiding centers are plotted as crosses. The abscissa is the corotation critical argument ( $\Psi_c = \lambda - \lambda_s$ , i.e., the azimuthal distance to the Lagrange satellite, see Table I), and the ordinate is the distance to the planet's center. The solid curves represent a typical tadpole, the separatrix, and a horseshoe orbit, respectively. Three different snapshots of the system have been plotted together (after 7, 61, and 73 revolutions, or 2737, 2896, and 3240 collisions, respectively). This diagram shows how inelastic collisions drive the particles away from the  $L_4$  point ( $\Psi_c = 60^\circ$ ,  $r = 1.0$ ). The particles cross the separatrix and then follow horseshoe orbits. Note that each particle is close to its guiding center because the eccentricity induced by collisions is small.

main in the libration zone, even after about 11,300 collisions, i.e., more than 220 collisions per particle (Fig. 8). We also see on this figure that in spite of its high eccentricity, the arc remains remarkably well confined. This is due to the combined effect of collisions and the forcing effect of the shepherd, which drives the particles in coherent

motion, on almost identical epicycles. This may appear paradoxical since collisions tend to destroy such coherent motion, but remember that the present system is *not* isolated because of the forcing effect of the shepherd.

Another result provided by Run F is that the average eccentricity of the particles increases monotonically with time. This is because the arc is at the exact location of the Lindblad resonance (see the dashed line in Fig. 8), so that the forced eccentricity  $e_0$  is infinite ( $\Delta n_s = 0$ , see Eq. (13)). In contrast, the torque density gradient is zero at the resonance, so that no energy is given to or removed from the guiding centers ( $\dot{\mathcal{E}}_c = 0$ , see Eq. (19)). This case is thus a typical example where all the energy provided by the shepherd is used to pump up the eccentricity of the arc.

#### 6.4. Arc at a Corotation Point of an Eccentric Satellite

The arc is now placed near an external corotation point 4:5 of a satellite  $S$  with orbital eccentricity  $e_s = 0.1$  and mass  $\varepsilon = 2 \times 10^{-5}$  (Run G). The same qualitative behavior as for Run F is observed. The arc remains relatively well confined around the corotation point, even after 6313 collisions (Fig. 9). A few particles escape however on circulating orbits. This occurs not because of dissipation of energy, but because the corotation potential is actually averaged over one synodic period. Thus high frequency terms in the disturbing potential can let the particle cross the separatrix. Otherwise, the same remarks as for the previous subsection apply: the eccentricities and the orbital phases of the particles tend to remain coherent in spite of the collisions. Moreover, the average eccentricity increases monotonously with time because the Lindblad

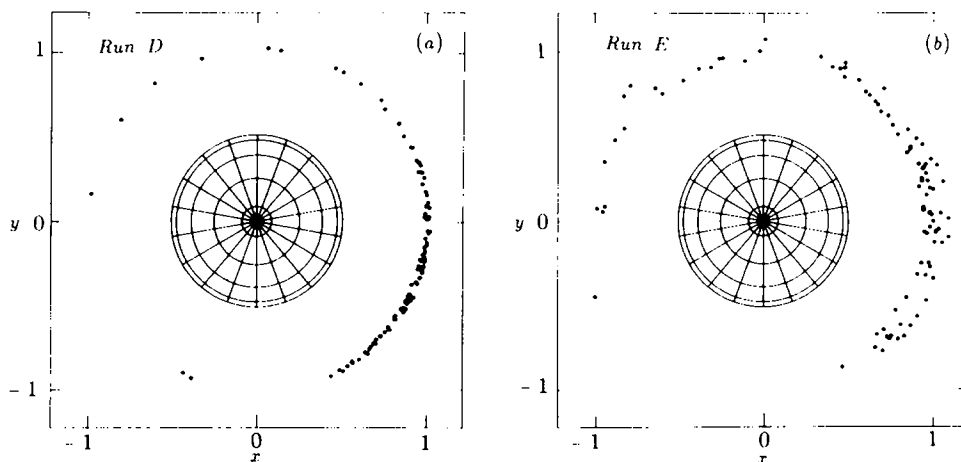


FIG. 7. (a) Run D, after 45 revolutions and 4100 collisions. The parameters are identical to those of Run C, except for the mass of the shepherd, which is now  $2 \times 10^{-5}$ , instead of zero. In spite of the presence of this shepherd, the energy given to the arc is still too small to prevent the spreading, see Fig. 3 for comparison. (b) Run E. This is a case where the energy provided by the shepherd is too large. The mass of the Lagrange satellite  $S$  is  $5 \times 10^{-4}$ , and the mass of the shepherd  $S'$  is  $2 \times 10^{-4}$ . After 28 revolutions and 437 collisions, the particles are given high eccentricities and escape on horseshoe orbits.

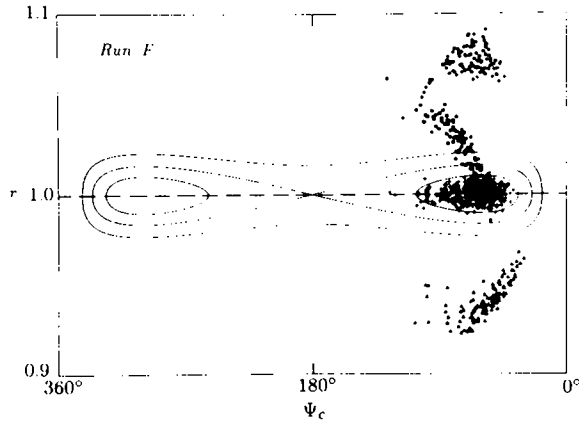


FIG. 8. Run F: this is an intermediate case between the Runs D and E shown in the previous figure. The Lagrange satellite has a mass  $10^{-4}$ , while the inner shepherd has a mass  $2 \times 10^{-5}$ . The inner satellite has a 4:5 Lindblad resonance whose location (dashed line) is coincident with the corotation radius. The particles (dots, squares, and triangles) are shown at three different moments (after 297, 306, and 316 revolutions, respectively, or 10,600, 10,900, and 11,300 collisions), together with their guiding centers (crosses). The shepherd forces a secularly increasing eccentricity on the arc, while the guiding centers remain well confined inside the separatrix. Note also that because of the coherent motion of the particles, the arc is at any moment well confined spatially. See Fig. 6 for comparison.

resonance radius (the dashed line in Fig. 9) lies right on the corotation radius.

### 6.5. Effect of the Torque Density Gradient

We now study the effect of the Lindblad resonance location on the arc stability. As we have noted in the previous subsection, if the Lindblad resonance radius co-

incides with the corotation radius, there is a secular increase of eccentricity, which eventually leads to the crossing of the shepherd orbit, and thus the destruction of the arc. Displacing the Lindblad resonance location yields a finite forced eccentricity (Eq. (13)), and thus prevents such an outcome. Furthermore, this creates a torque density gradient across the arc, which can stabilize, or destabilize the arc, as discussed in Section 3.4.

In order to test this effect, we displace the Lindblad resonance radius with respect to the corotation radius. In the first configuration (two satellites on circular orbits), it is enough to change the inner satellite semi-major axis to change accordingly the Lindblad resonance radius. In the second case (a single satellite on an eccentric orbit), the splitting between the two resonances requires that an apsidal motion  $\dot{\omega}_s$  be given to the satellite (see Eq. (9)). In our simulations, the value and sign of  $\dot{\omega}_s$  do not correspond to the particular value induced by Neptune's oblateness. Rather, this parameter has an arbitrary value, which is intended to test the stabilizing, or destabilizing, effect of the Lindblad resonance.

In the first two runs examined here, all the parameters are the same, except for the semi-major axis of the shepherd (see Table II). In one case (Run H), the Lindblad resonance radius is at the distance 0.0069 *outside* the corotation radius, and in the other case (Run I), it lies at the distance 0.0069 *inside* the corotation radius. The position of the Lindblad resonance is shown as dashed lines in Figs. 10 and 11. As expected from the discussion of Section 3.4, the torque density gradient across the arc is positive in Run H, so that the arc should be unstable. This is verified in Fig. 10, where the arc is shown when it is about to disrupt, after 35 revolutions and 1260 collisions. In Run I on the contrary, the torque density gradient

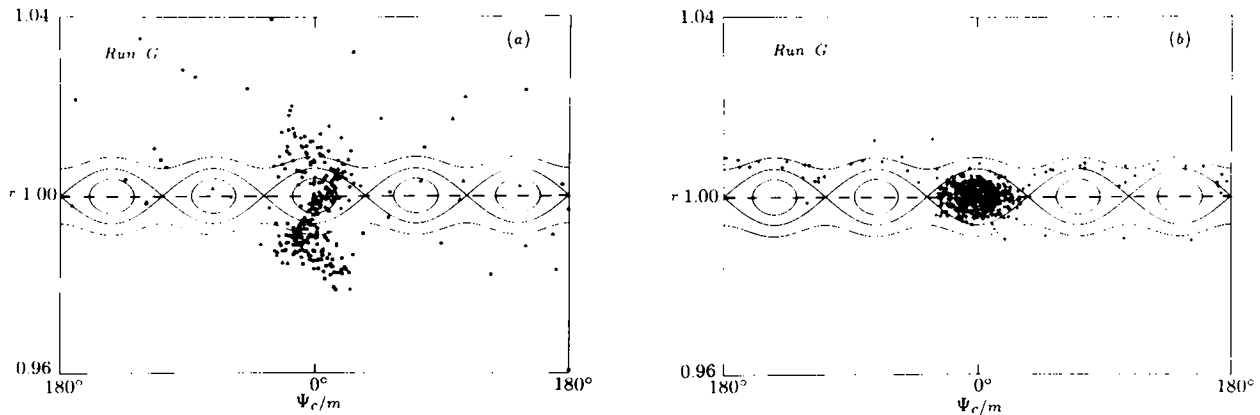


FIG. 9. The same as Fig. 8, but with a single eccentric satellite (Run G). The corotation critical argument is now  $\Psi_c = (m + 1)\lambda_s - m\lambda - \dot{\omega}_s$  (see Table I). The dashed line shows the location of the Lindblad resonance, coincident with the corotation radius. (a) The particles have been plotted after 58, 89, and 96 revolutions, or 3406, 5840, and 6313 collisions (dots, square, and triangles, respectively). (b) The corresponding positions of the guiding centers. The same qualitative behavior as in Fig. 8 is observed: the particles follow a coherent eccentric motion while the guiding centers are locked around the stable corotation point.

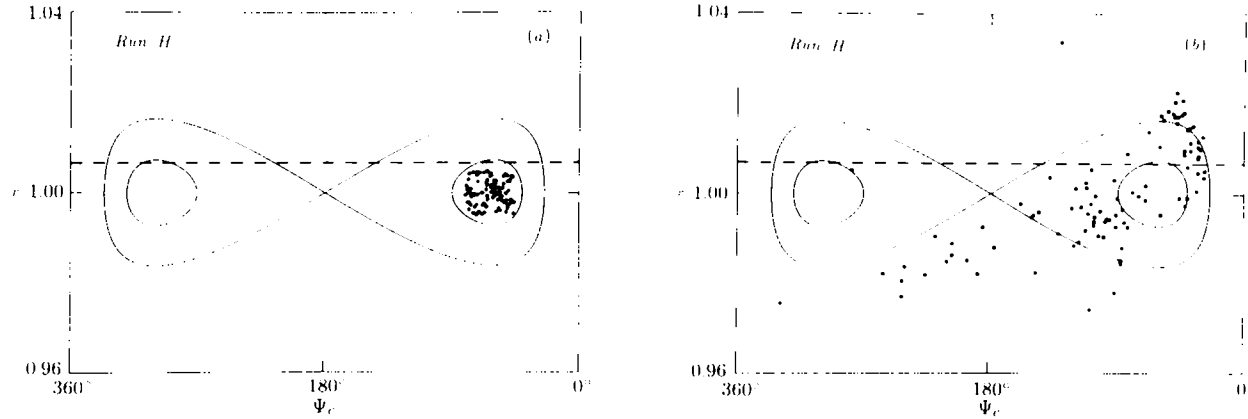


FIG. 10. The effect of the torque density gradient. Run H has the same parameters as Run F, except that the mass of the shepherd has been increased to  $1.3 \times 10^{-4}$ , and that the Lindblad resonance (dashed line) has been shifted *outward* by a distance of 0.0069, so as to create a torque density gradient across the arc. (a) Initial conditions. (b) The guiding centers of the particles after 35 revolutions and 1260 collisions, when the arc is being disrupted. See Fig. 8 for comparison.

is negative, and the arc is stabilized, as shown in Fig. 11, after 153 revolutions and 10,425 collisions.

Figure 12 shows the evolution of the arc in the energy–eccentricity diagram, for Runs H and I. In Run H, the particles are driven away from the libration region, their eccentricities increase, and they eventually cross the separatrix. In Run I, the points representing the arc go back and forth against the forbidden region, indicating that the guiding centers are locked on the maximum of potential, while the particles have a forced, coherent motion with finite eccentricity (see also Fig. 11). Thus, the arc reaches a limit cycle where the energy provided by the shepherd is dissipated by collisions.

In Fig. 13, the  $k$  component of the eccentricity vector of each particle is plotted as a function of the distance  $\xi$

of the guiding center to the corotation radius. Remember that  $k$  represents also the opposite of the torque exerted on each particle, according to Eq. (16). We can check that in the unstable case (Run H, Fig. 13a), the torque gradient is positive, while it remains negative in the stable case (Run I, Fig. 13b).

Runs J and K are the equivalent of Runs H and I in the case where there is only one satellite with an eccentric orbit. The parameters used in these two runs are identical, except for the apsidal precession rate  $\dot{\omega}_s$ , which has been adjusted so that the Lindblad resonance lies at the distance 0.004 *outside* the corotation radius for Run J, and at the distance 0.004 *inside* the corotation radius for Run K (see Table II). The same qualitative behavior as for Runs H and I is observed. When the Lindblad resonance is

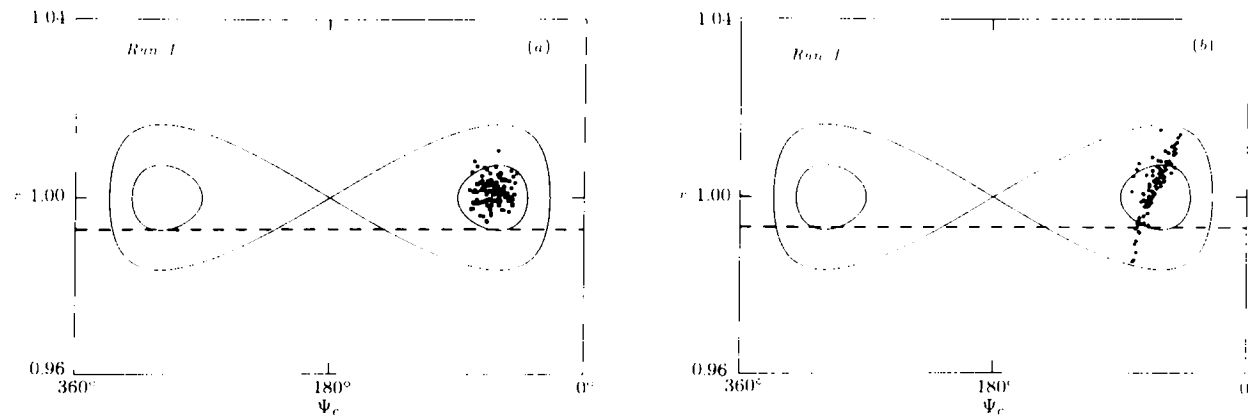


FIG. 11. Effect of the torque density gradient. Run I: identical to Run H shown in Fig. 10, except that the Lindblad resonance (dashed line) has been moved *inside* the corotation radius by the distance 0.0069, so that to change the sign of the torque density gradient with respect to Fig. 10. The arc is shown after 153 revolutions and 10,425 collisions. (a) The guiding centers are locked inside a tadpole orbit. (b) The particles themselves follow coherent motions, with a finite forced eccentricity.

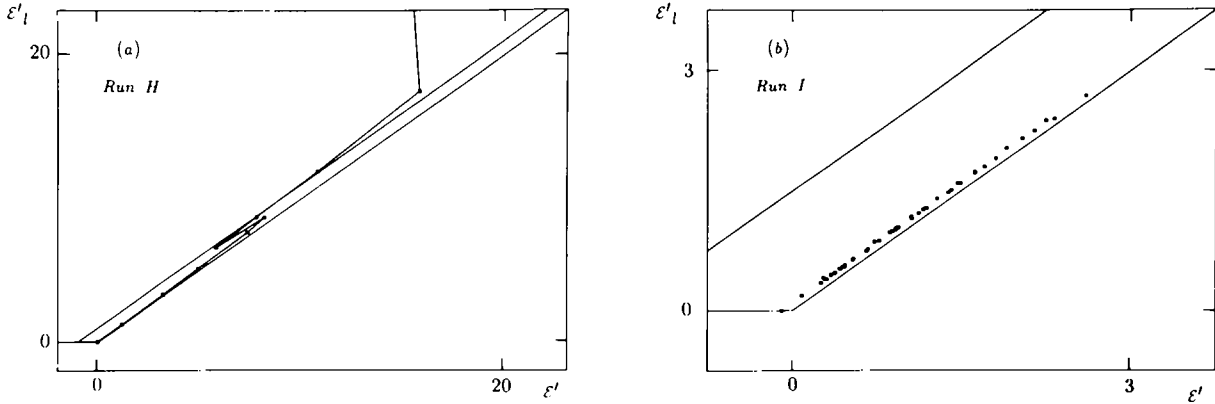


FIG. 12. Evolution of the arc in the energy–eccentricity diagram. (a) Run H: energy is removed from the particle guiding centers, which eventually cross the separatrix. Note, however, that energy is given to the arc under the form of eccentric motion. (b) Run I: the average value of  $\epsilon'$  and  $\epsilon'_l$  of the particles have been plotted at different times (from 0 to 160 revolutions). The points go back and forth against the forbidden region, indicating that a limit cycle is reached, where the energy provided by the inner satellite (essentially under the form of eccentric motion) is dissipated by collisions.

outside the corotation radius, the arc is rapidly destroyed (Run J, Fig. 14a), while it remains stable in the opposite case (Run K, Fig. 14b). Figure 15 shows the arc in the energy–eccentricity diagram in both cases. Again, the particles are driven toward the separatrix in the unstable case, and they are trapped in a limit cycle in the stable case.

7. DISCUSSION

Our main analytical results are contained in Eqs. (6), (10), and (12), which describe the motion of a particle

near a corotation resonance, and perturbed by a Lindblad resonance. On the other hand, Eq. (19) gives the rate of transfer of energy from the Lindblad resonance to the guiding centers of the particles in the arc. Our analytical results are tested with a direct numerical simulation, which takes into account inelastic collisions between finite size particles. Our numerical results are summarized in Fig. 16. These two different approaches show that

- The motion of a particle near a corotation resonance and a Lindblad resonance may be described by two coupled dynamical systems, namely a simple pendulum and

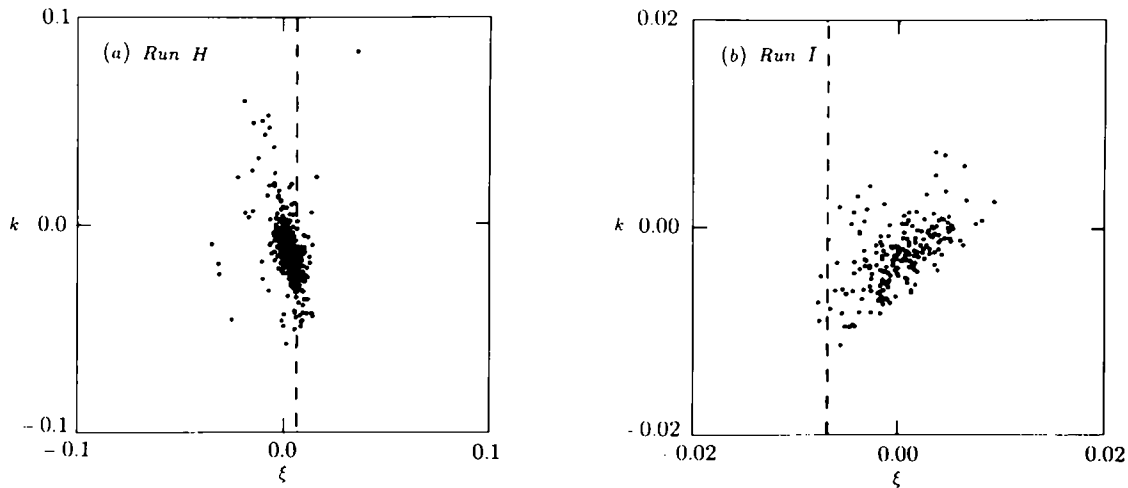


FIG. 13. Evidence for a gradient of torque density across the arc. For each particle, the value of  $k$  (proportional to the opposite of the torque density, see Eq. (16)) is plotted against  $\xi$ , the dimensionless distance to the corotation radius. (a) Run H: when the Lindblad resonance (dashed line) is outside the arc, the gradient of  $k$  is negative (i.e., the gradient of torque density is positive), and the arc is destroyed. The values of  $k$  against  $\xi$  are plotted here before the arc is destroyed, after 19 revolutions and 1054 collisions. (b) Run I: in the opposite case, the gradient of  $k$  is positive, which ensures the arc stability (Eq. (19)). The diagram is shown after 157 arc revolutions, and 10,682 collisions. Note the change of scale between (a) and (b).

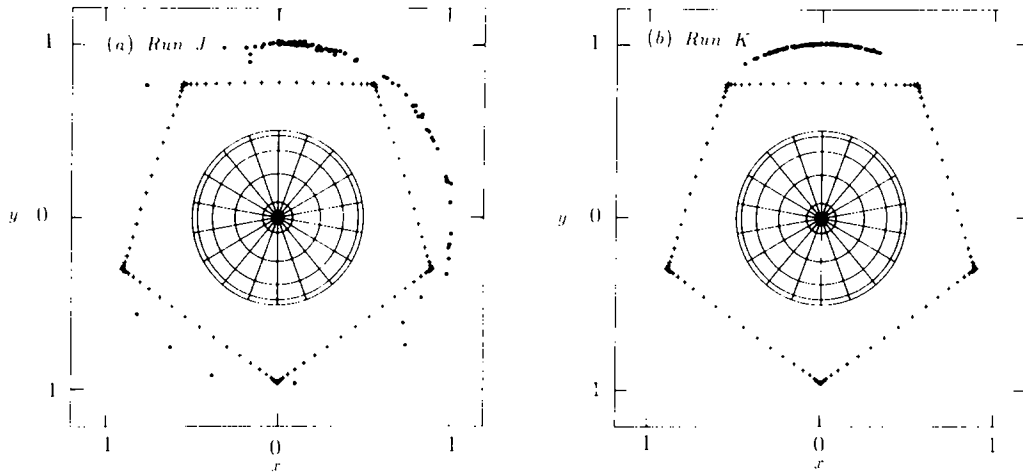


FIG. 14. Stability of the arc with a single satellite on an eccentric orbit. The mass of the satellite is  $7 \times 10^{-5}$ . (a) Run J: due to the precession rate  $\dot{\omega}_p$  of the satellite's orbit periaipse, the Lindblad resonance is shifted at a distance 0.004 *outside* the corotation radius (see Table II). The arc, shown here after 112 revolutions and 6236 collisions, is being disrupted. (b) Run K: everything equal besides, the periaipse precession rate has the opposite value (Table II), so that the Lindblad resonance is now at 0.004 *inside* the arc. The arc, shown after 157 revolutions and 8423 collisions, is then stabilized.

a harmonic oscillator. The coupling between the two motions is determined by collective effects in the arc.

- Equation (19) gives the part of the energy provided by the Lindblad resonance, used to confine the arc, that is, used to maintain the guiding centers of the particles at the maximum of potential created by the corotation resonance. This energy is positive, i.e., the arc is stable is, if the *gradient* of the torque density across the arc is negative. As a consequence, the position of the Lindblad resonance relative to the corotation radius determines the arc stability. More precisely, an outer (inner) Lindblad resonance should be inside (outside) the arc for the latter to be stable. This confirms previous work by Lissauer (1985), where the resonances overlap, and by Lin, Pa-

paloizou, and Ruden (1987), where the resonances are isolated. However, our analysis shows that the response of the arc to the Lindblad resonance may be complicated by the presence of waves. In this case, a more careful evaluation of the integral in Eq. (19) must be done to decide whether the resonance stabilizes or destabilizes the arc.

- The numerical simulation shows that dissipation of energy through collisions is responsible for the azimuthal spreading of an arc (Fig. 3). This confirms previous analytical work on the stability of Lagrange (see, for instance, Greenberg and Davis 1978).

- The arc stability is tested in our simulation by displacing the Lindblad resonance with respect to the corotation

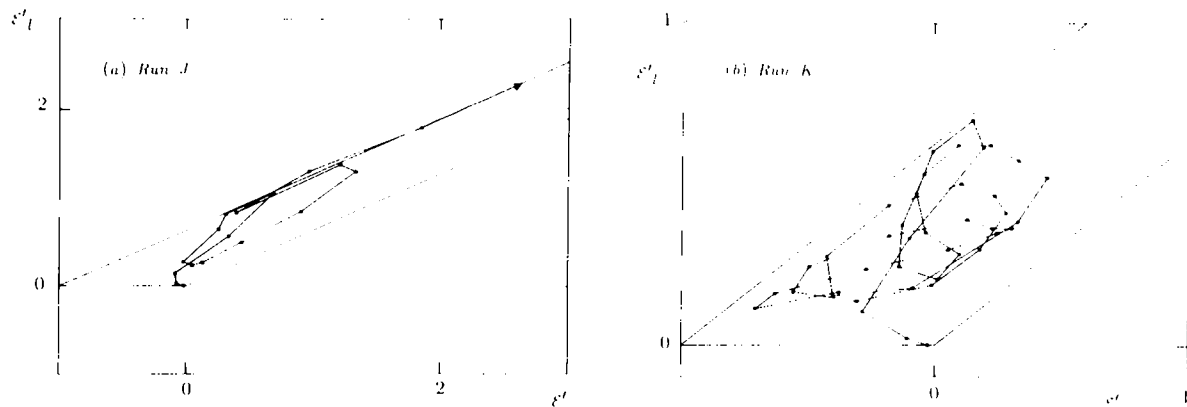


FIG. 15. Equivalent to Fig. 12, but with a satellite on an eccentric orbit. (a) Run J: the arc escapes the libration region after about 70 revolutions and 4240 collisions, because of the negative gradient of  $k$  across the libration region (see Figs. 12a and 14a for comparison). (b) Run K: the arc reaches a limit cycle, and is trapped in the libration region. The total number of revolutions of the arc is 157, and the total number of collisions is 8423 (see also Figs. 12b and 14b).

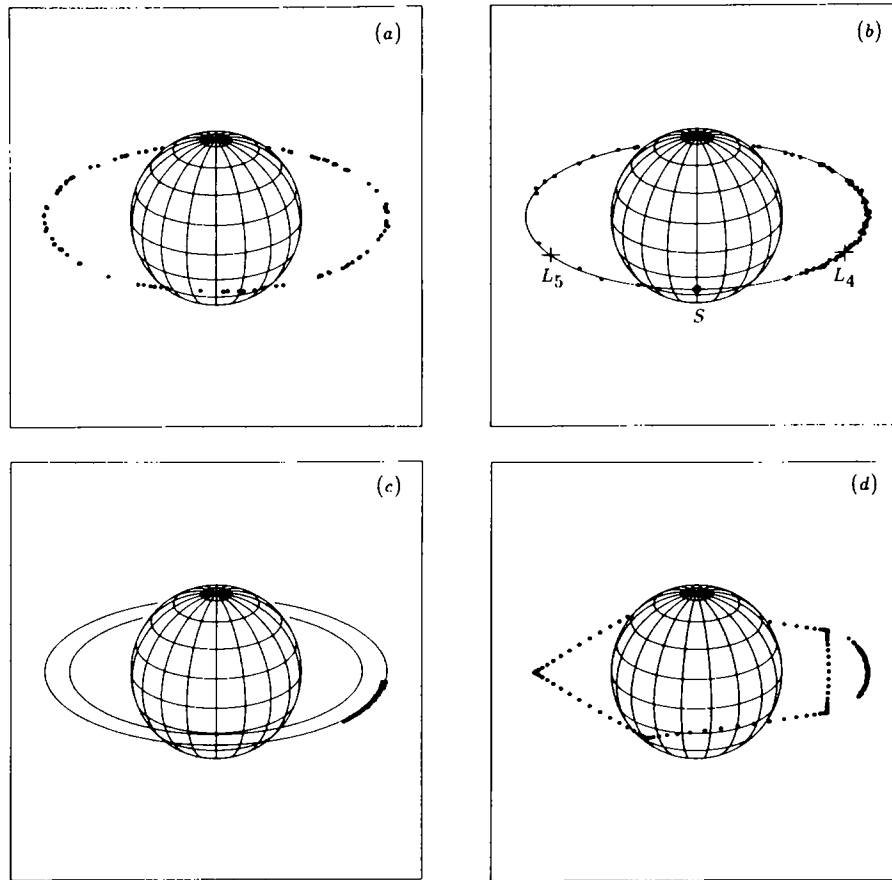


FIG. 16. Summary. (a) Run A: a free arc spreads very rapidly due to the Keplerian differential motion. (b) Run C: a corotation resonance may slow this spreading, but dissipation of energy destroys the arc because corotation points are maxima of potential energy. (c) Run I: a second satellite may confine the arc, provided that the torque density decreases outward (negative gradient of the torque density). Otherwise, the arc is destroyed, see Fig. 10. (d) Run K: the same kind of confinement may be achieved with only one eccentric satellite. Again, the gradient of torque density across the arc must be negative for the latter to be stable, otherwise the arc is destroyed (Fig. 14a).

radius. The two cases investigated here (two satellites on circular orbits, or one satellite on eccentric orbit) show a similar dynamical behavior. In particular we confirm that the arc is confined if the gradient of the torque density across the arc is negative (Figs. 11 and 14).

Our simulation is focused on the role of inelastic collisions only, so that self-gravitation, Poynting–Robertson effects, and plasma drag, among others, are ignored. Several points have not been addressed in this paper, and they should be nevertheless important for a better knowledge of planetary arcs. Without being exhaustive, we can note the following:

Equation (19) allows one, in principle, to make an energy budget of the arc and thus, to decide whether the latter is stable or not against collisions. However, this budget depends on physical parameters whose values are still poorly known in the case of Neptune arcs (pressure, viscosity, velocity dispersion, self-gravitation, coefficients of restitution, effect of particle spin, plasma drag,

Poynting–Robertson effect, etc.). More detailed analysis of Voyager 2 observations could fill some of these gaps.

Collective effects in the arc are essentially due to big particles, which contain most of the mass of the arc, while the photometric properties of the arc are dominated by microscopic particles. The latter are submitted to non-gravitational forces like Poynting–Robertson drag and/or plasma drag, so that they can escape confinement. A direct integration of the orbit, or the use of the averaged equations of motion (Eqs. (6), (10), and (12)), where dissipative forces are accounted for, would be most useful to assess the importance of nongravitational forces on grains.

The present work has been developed in a frame where the standard shepherding mechanism applies, i.e., assuming that there are frequent interactions between arc particles. This may be not the case for Neptune’s arcs, if most of the mass is contained in very few big particles with little interactions, while most of the optical depth is accounted for by small (dust) particles. Such a model would

deserve a study of its own, after more detailed analysis of the Voyager 2 images has been done.

Other problems in the Solar System could receive a new insight as Neptune's arcs are probed. We can think of dust trapped near corotation points of satellites or planets, accretion processes near corotation resonances in the early history of the Solar Nebula, and the formation and evolution of the Trojan asteroids or coorbital satellites.

## APPENDIX A

### List of Symbols

$A$ : a combination of Laplace coefficients, see Table I.  
 $a, a_s$ : semi-major axis of the orbit of the test particle, of the satellite.  
 $a_0$ : reference semi-major axis defining the corotation radius.  
 $b_{lm}^{(m)}$ : Laplace coefficient.  
 $c$ : velocity dispersion among the particles of the arc.  
 $E$ : a combination of Laplace coefficients, see Table I.  
 $E_s$ : mechanical energy of the test particle in an inertial frame.  
 $e, e_s$ : eccentricity of the orbit of the test particle, of the satellite.  
 $e_0$ : the forced eccentricity near a Lindblad resonance.  
 $\mathcal{E}$ : mechanical energy of the test particle in a frame corotating with the particle.  
 $\mathcal{E}_c, \mathcal{E}_l$ : parts of  $\mathcal{E}$  associated to the corotation and the Lindblad resonances, respectively. Note that  $\mathcal{E} = \mathcal{E}_c + \mathcal{E}_l$ .  
 $\mathcal{E}', \mathcal{E}'_l$ : dimensionless expressions of  $\mathcal{E}$  and  $\mathcal{E}_l$ . See Eqs. (21) for definition.  
 $f(\Psi_c) = \cos(\Psi_c) - 1/2\sin(\Psi_c/2)$ : the function describing the variation of the potential energy along the satellite orbit. The extrema of  $f$  give the positions of the Lagrange points  $L_3, L_4$ , and  $L_5$ .  
 $\bar{\mathcal{T}}_m$ : a dimensionless coefficient depending on  $m$ . Used for calculating the standard torque at a Lindblad resonance.  
 $G$ : gravitational constant.  
 $H_l$ : angular momentum of the test particle in an inertial frame.  
 $h = e \cos(\Psi_l)$ : the first component of the eccentricity vector  $\vec{e}$ .  
 $i, i_s$ : inclination of the orbit of the test particle, of the satellite.  
 $J_2$ : dynamical oblateness of the planet.  
 $k = e \sin(\Psi_l)$ : the second component of the eccentricity vector  $\vec{e}$ .  
 $k_r, k_t$ : radial and tangential rebound coefficients, respectively, for two colliding particles.  
 $L$ : length of the arc.  
 $L_1, \dots, L_5$ : Lagrange equilibrium points of the circular three body problem.  
 $M_A, M_p, M_S, M_T$ : masses of the arc, the planet, the satellite, and the test particle, respectively.  
 $m$ : integer defining the resonance condition  $n/n_s = (m+1)/m$ .  
 $N$ : number of particles used in the numerical simulation.  
 $n, n_s$ : mean motions of the test particle and of the satellite.  
 $n_0$ : mean motion at radius  $a_0$ .  
 $R_p$ : equatorial radius of the planet.  
 $\vec{r}, \vec{r}_s$ : position vector of the test particle and of the satellite, respectively.  
 $s, s'$ : subscripts referring to satellites  $S$  and  $S'$ , respectively.  
 $T_c$ : period of the libration motion associated to the corotation resonance.  
 $T_{orb}$ : orbital period.  
 $T$ : subscript referring the test particle.  
 $V$ : a combination of Laplace coefficients, see Table I.  
 $w$ : radial width of the arc.  
 $\alpha$ : a dimensionless coefficient describing the response of a disk near

a resonance. It depends on physical parameters like pressure, viscosity, density, etc.

$\beta = a/a_s$ : ratio of the semi-major axis of the test particle orbit to the semi-major axis of satellite  $S$  orbit.

$\beta' = a'/a_s$ : Id. with satellite  $S'$ .

$\beta_0 = a_0/a_s$ : see the definition of  $a_0$ .

$\Gamma$ : torque exerted by the satellite on the test particle.

$\vec{\Delta} = \vec{r} - \vec{r}_s$ : relative position vector of the test particle w.r.t. the satellite.

$\epsilon = M_S/M_p$ : ratio of the mass of satellite  $S$  to the mass of the planet.

$\epsilon' = M_{S'}/M_p$ : Id. for satellite  $S'$ .

$\lambda, \lambda_s$ : mean longitude of the particle, of the satellite.

$\xi = (a - a_0)/a$ : the dimensionless distance to the corotation radius.

$\rho$ : radius of the arc particles.

$\Sigma_0$ : the unperturbed surface density of the ring-like arc material.

$\tau$ : normal optical depth of the arc.

$\Phi$ : total potential energy of the test particle, per unit mass.

$\Phi_s$ : potential energy of the test particle due to the interaction with the satellite, per unit mass.

$\Psi_c, \Psi_l$ : critical arguments of corotation and Lindblad resonances, respectively, see Table I.

$\Omega, \Omega_s$ : longitude of the node of the orbit of the test particle, of the satellite.

$\omega, \omega_s$ : longitude of the periaipse of the orbit of the test particle, of the satellite.

## ACKNOWLEDGMENTS

It is a pleasure to thank Sylvio Ferraz-Mello for patient explanations on resonance dynamics. I thank Peter Goldreich for several discussions at the California Institute of Technology, where part of this work was done. I am grateful to Joseph A. Burns for his hospitality at Cornell University, where part of the numerical work was achieved, under the support of a NASA grant. I thank Jack J. Lissauer for discussion during the revision of this paper. The detailed comments of two referees were most useful for improving this paper. Finally, I have benefited from the computing facilities allocated by the "Centre de Calcul Vectoriel pour la Recherche" (Palaiseau, France), which gave me access to the Cray 1 computer.

## REFERENCES

- BRAHIC, A. 1976. Numerical simulation of a system of colliding bodies in a gravitational field. *J. Comp. Phys.* **22**, 171–188.
- BRAHIC, A. 1977. Systems of colliding bodies in a gravitational field: I. Numerical simulation of the standard model. *Astron. Astrophys.* **54**, 895–907.
- BRAHIC, A., AND M. HÉNON 1977. Systems of colliding bodies in a gravitational field: II. Effects of transversal viscosity. *Astron. Astrophys.* **59**, 1–7.
- BRAHIC, A., SICARDY, B., ROQUES, F., MCLAREN, R., AND W. B. HUBBARD 1986. Neptune's arcs: Where and how many? *Bull. Amer. Astron. Soc.* **18**, 778.
- BROUWER, D., AND G. H. CLEMENCE 1961. *Method of Celestial Mechanics*. Academic Press, New York.
- COVAULT, C. E., GLASS, I. S., FRENCH, R. G., AND J. L. ELLIOT 1986. The 7 and 25 June 1985 Neptune occultations: Constraints on the putative Neptune "arcs." *Icarus* **67**, 126–133.
- DERMOTT, S. F. 1984. Dynamics of narrow rings. In *Planetary Rings* (R. Greenberg and A. Brahic, Eds.) pp. 589–637. Univ. Ariz. Press, Tucson.

- FERRAZ-MELLO, S. 1987. Averaging the elliptic asteroidal problem near a first-order resonance. *Astron. J.* **94**, 208–212.
- GOLDREICH, P., AND S. TREMAINE 1980. Disk-satellite interactions. *Astrophys. J.* **241**, 425–441.
- GOLDREICH, P., AND S. TREMAINE 1982. The dynamics of planetary rings. *Annu. Rev. Astron. Astrophys.* **20**, 249–283.
- GOLDREICH, P., TREMAINE, S., AND N. BORDERIES 1986. Towards a theory for Neptune arc rings. *Astron. J.* **92**, 490–494.
- GREENBERG, R., AND D. R. DAVIS 1978. Stability at potential maxima: The  $L_4$  and  $L_5$  points of the restricted three-body problem. *Amer. J. Phys.* **46**, 1068–1070.
- HUBBARD, W. B., BRAHIC, A., SICARDY, B., ELICER, L. R., ROQUES, F., AND F. VILAS 1986. Occultation detection of a Neptunian ring-like arc. *Nature (London)* **319**, 636–640.
- HUBBARD, W. B. 1986. 1981 N1: A Neptune arc? *Science* **231**, 1276–1278.
- HUBBARD, W. B., RIEKE, G. H., RIEKE, M. J., MARCIALIS, R., AND H. CAMPINS 1987. Coincidence search for Neptunian ring arcs. *Bull. Amer. Astron. Soc.* **19**, 885.
- LIN, D. N. C., PAPALOIZOU, J. C. B., AND S. P. RUDEN 1987. On the confinement of planetary arcs. *Mon. Not. R. Astron. Soc.* **227**, 75–95.
- LISSAUER, J. J. 1985. Shepherding model for Neptune's arc ring. *Nature (London)* **318**, 544–545.
- MEYER-VERNET, N., AND B. SICARDY 1987. On the physics of resonant disk-satellite interaction. *Icarus* **69**, 157–175.
- NICHOLSON, P. D., COOKE, M. L., MATTHEWS, K., ELIAS, J. H., AND G. GILMORE 1990. Stellar occultations by Neptune: Further evidence for incomplete arcs. *Icarus* **87**, 1–39.
- PEALE, S. J. 1986. Orbital resonances, unusual configurations and exotic rotation states among planetary satellite. In *Satellites* (J. A. Burns and M. S. Matthews, Eds.) pp. 159–223. Univ. of Arizona Press, Tucson.
- REITSEMA, H. J., HUBBARD, W. B., LEBOSKY, L. A., AND D. J. THOLEN 1982. Occultation by a possible third satellite of Neptune. *Science* **215**, 289–291.
- SHU, F. H. 1984. Waves in planetary rings. In *Planetary Rings* (R. Greenberg and A. Brahic, Eds.) pp. 513–561. Univ. of Arizona Press, Tucson.
- SICARDY, B., BOUCHET, P., BRAHIC, A., McLAREN, R., PERRIER, C., AND F. ROQUES 1985. The 20 August 1985 stellar occultation by Neptune and its arc system. *Bull. Amer. Astron. Soc.* **17**, 923–924.
- SICARDY, B., ROQUES, F., BRAHIC, A., BOUCHET, P., MAILLARD, J. P., AND C. PERRIER 1986. More dark matter around Uranus and Neptune? *Nature (London)* **320**, 729–731.
- SICARDY, B. 1988. *Etude observationnelle, analytique et numérique des environnements planétaires. Applications aux anneaux de Saturne et d'Uranus et aux arcs de Neptune*. Thèse de doctorat d'état ès sciences physiques, Univ. Paris 7.
- SICARDY, B. 1991. Numerical experiment of perturbed collisional disks. *J. Comp. Phys.*, submitted for publication.
- SICARDY, B., ROQUES, F., AND A. BRAHIC 1991. Neptune's rings, 1983–1989: Ground-based stellar occultation observations. I. Ring-like arc detections. *Icarus* **89**, 220–243.
- SMITH, B. A., SODERBLUM, L. A., BANFIELD, D., BARNET, C., BASILEVSKY, A. T., BEFBE, R. F., BOLLINGER, K., BOYCE, J. M., BRAHIC, A., BRIGGS, G. A., BROWN, R. H., CHYBA, C., COLLINS, S. A., COLVIN, T., COOK II, A. F., CRISP, D., CROFT, S. K., CRUIKSHANK, D., CUZZI, J. N., DANIELSON, G. E., DAVIES, M. E., DE JONG, E., DONES, L., GODFREY, D., GOGUEN, J., GRENIER, I., HAEMMERLE, V. R., HAMMEL, H., HANSEN, C. J., HELFENSTEIN, C. P., HOWELL, C., HUNT, G. E., INGERSOLL, A. P., JOHNSON, T. V., KARGEL, J., KIRK, R., KUEHN, D. I., LIMAYE, S., MASURSKY, H., McEWEN, A., MORRISON, D., OWEN, T., OWEN, W., POLLACK, J. B., PORCO, C. C., RAGES, K., ROGERS, P., RUDY, D., SAGAN, C., SCHWARTZ, J., SHOEMAKER, E. M., SHOWALTER, M., SICARDY, B., SIMONELLI, D., SPENCER, J., SROMOVSKY, L. A., STOKER, C., STROM, R. G., SUOMI, V. E., SYNOTT, S. P., TERRILE, R. J., THOMAS, P., THOMSON, W. R., VERBISCHER, A., AND J. VEVERKA 1989. Voyager 2 at Neptune: Imaging science results. *Science* **246**, 1422–1449.